

ABSTRACT

Title of Thesis: STUDY OF SPACE-CHARGE WAVES IN A LONG SOLENOID CHANNEL

Kai Tian, Master of Science, 2005

Thesis Directed By: Professor Patrick O'Shea
Department of Electrical and Computer Engineering

In this thesis, studies of the dynamics of longitudinal space-charge waves in space-charge dominated beams propagating through a transport channel with a long solenoid are performed. First, some basic models of space-charge waves behaviors are reviewed. Second, WARP simulations on generating either pure fast waves or pure slow waves are presented. Then experimental studies on the energy modulations converted from density modulations are reported. By changing the working conditions of the electron gun, pure initial density modulations are generated. Energy perturbation waveforms are measured by a high resolution energy analyzer. Finally, the experimental results are compared with both the linear theory and the WARP simulation results. Good agreements are achieved for the relationship between the energy and current perturbation strengths. The notable exception is a large discrepancy between experiment and theory for the speed of sound at differing perturbation strengths, which remains to be investigated in future work.

STUDY OF SPACE-CHARGE WAVES IN A LONG SOLENOID CHANNEL

By

Kai Tian

Thesis submitted to the Faculty of the Graduate School of the
University of Maryland, College Park, in partial fulfillment
of the requirements for the degree of
Master of Science
2005

Advisory Committee:

Professor Patrick O'Shea, Chair / Advisor
Professor Emeritus Martin Reiser
Professor Victor L. Granatstein
Doctor Rami A. Kishek

© Copyright by
Kai Tian
2005

Dedication

to my wife, Qiushi Lu

Acknowledgements

First, I would like to thank my advisor, Professor Patrick G. O'Shea, who guided me to achieve the successful completion of my thesis. I would express my appreciation to him not only for his professional advice and guidance, but also for his enthusiasm and encouragement. I also thank his generosity for providing funding support for my research. I would like to express my thanks to Professor Martin Reiser who is the senior authority in our field. I always benefit from his constructive criticism on my work.

I would like to thank Dr. Yun Zou, the former Research Scientist in the UMER lab, for his invaluable help in both theoretical and experimental parts of my dissertation. I would like to thank Dr. Yupeng Cui for his contribution to the experimental system setup and help in the experimental part of my thesis. I am most grateful to Dr. Rami Kishek and Dr. Irving Haber for their help on my simulation work. I would like to thank Dr. M. Walter for his mechanical support and Mr. Bryan Quinn for his valuable suggestions and support on electrical problems.

I wish to thank Professor V. Granatstein for serving on my thesis exam committee.

Table of Contents

Dedication	ii
Acknowledgements.....	iii
Table of Contents.....	iv
List of Tables	vi
List of Figures.....	vii
Chapter 1 Introduction	1
1.1 History and background.....	1
1.2 Motivation.....	5
Chapter 2 Theory and Simulation of Space-charge Waves	8
2.1 Single particle dynamics in a sinusoidal density modulation beam	8
2.2 Analysis of Space-charge waves using the One Dimensional Fluid Model	11
2.3 Analytical condition for generating pure slow wave or fast wave.....	13
2.4 Generation of pure fast or slow wave perturbation in WARP Simulations.....	16
Chapter 3 Experiment study on the space-charge wave evolution	22
3.1 Experimental setup for the study of the space-charge wave.....	22
3.1.1 Introduction.....	22
3.1.2 Description of the Electron Gun	25
3.1.3 Energy Analyzer	28
3.1.4 Solenoids.....	31
3.2 Experimental study on the localized density modulation evolution	32
3.2.1 Generation of a localized pure current perturbation at the gun	32

3.2.2 Measurement of energy perturbation with energy analyzer	34
3.3 Experiment result analysis and comparison with theory and simulation.....	39
3.3.1 Import the beam current into WARP.....	39
3.3.2 Comparison of the wave shapes for the mean energy along the beam	42
3.3.3 Relation between the strengths of initial current perturbation and final energy perturbation achieved.....	44
3.3.4 Comparisons of the space-charge wave velocity	47
Chapter 4 Conclusion.....	50
References:.....	52

List of Tables

<i>Table 3.1 Data for the solenoids</i>	31
<i>Table 3.2 Data for current perturbation generation at the gun</i>	33
<i>Table 3.3 Beam parameters setting in WARP</i>	40
<i>Table 3.4 Energy perturbation peak-to-peak strengths and η</i>	45
<i>Table 3.5 Sound speed calculated from theory and experiment</i>	49

List of Figures

<i>Figure 2.1 current perturbation evolution in WARP with $\delta=0.003$ $\eta=0.04417$.....</i>	<i>18</i>
<i>Figure 2.2 Velocity perturbation evolution in WARP with $\delta=0.003$ $\eta=0.04417$.....</i>	<i>19</i>
<i>Figure 2.3 Current perturbation evolution in WARP with $\delta=0.003$ $\eta=-0.03817$.....</i>	<i>20</i>
<i>Figure 2.4 velocity perturbation evolution in WARP with $\delta=0.003$ $\eta=-0.03817$.....</i>	<i>21</i>
<i>Figure 3.1 schematic of the long transport line experimental setup</i>	<i>24</i>
<i>Figure 3.2 Photo of the long transport line experimental setup.....</i>	<i>24</i>
<i>Figure 3.3 Circuit diagram for the electron gun</i>	<i>27</i>
<i>Figure 3.4 (a) mechanical schematic of the energy analyzer (b) electrical circuit of this energy analyzer</i>	<i>29</i>
<i>Figure 3.5 Four groups of initial currents with perturbation</i>	<i>33</i>
<i>Figure 3.6 Current signals acquired by energy analyzer with different retarding voltage in Group 3</i>	<i>35</i>
<i>Figure 3.7 (a) the red curve represent the current versus retarding voltage and the blue curve is the energy spectrum before smoothing (b) data after smoothing.....</i>	<i>36</i>
<i>Figure 3.8 Mean energy waveforms derived from energy analyzer signals for different groups</i>	<i>38</i>
<i>Figure 3.9 Current profile imported into WARP in Group 3</i>	<i>41</i>
<i>Figure 3.10 Comparisons of the wave form of mean energy for the experiment results, WARP simulation results and one-dimensional cold fluid theory</i>	<i>43</i>
<i>Figure 3.11 The relationship between the energy perturbation strength and initial current perturbation strength. The black dots represent experiment data, the green</i>	

squares represent the WARP simulation results, the red stars represent analytical solution from one-dimensional cold fluid theory..... 46

Figure 3.12 Comparison of sound speed between theory and experiment..... 49

Chapter 1 Introduction

1.1 History and background

Charged particle beams have been used in many diverse areas of scientific research and industrial applications [1], such as electron microscopes, cathode ray tubes (CRT) and particle accelerators. The physics of low intensity beams has been well studied since the 1920's. However, the recent interest in heavy ion fusion (HIF) [2-4], the developments of the spallation neutron source [5] and free electron lasers (FEL) [6], require more detailed knowledge and understanding of the physics of the high intensity beams in which space-charge forces play a much more important role than in conventional accelerators, such as the existing high-energy collider rings. As an example, the proposed current of heavy ion beams for HIF is about 4000 A and will be focused to a spot of a few millimeters radius at the target. Although the beam can be partly neutralized before the target in order to reduce the space-charge effects, they will still play a crucial role in the early part of the induction Linac by affecting the transportation, acceleration and compression of the beam. The physics of all the initial experimental and theoretical studies on inertial confinement fusion with intense beams carried out in the U.S., Europe, Russia and Japan are characterized by very intense, space-charge dominated beams. Indeed, all the beams are born as space-charge dominated beams at the gun. Therefore, to understand the physical nature of the space-charge dominated beams is an important task for today's physicists and

researchers.

In the space-charge dominated beams, the nonlinear space-charge forces will introduce many collective effects, which may limit the maximum transportation current or beam quality. Some of these collective behaviors are not well understood. One of the effects is the longitudinal space-charge waves, which can be generated by the density perturbation or energy perturbation. These perturbations can be excited by many factors in actual machines, such as the discontinuity of the beam transportation modules, fluctuations in the bunch, or the mismatch of the external focusing channels. Longitudinal instabilities in the beams can be excited by the interactions among the space-charge waves and the external transport and acceleration environment, such as resistive wall channel.

There is a long history for the research on the behaviors of space-charge waves in the field of microwave generation, which can be traced back to the 1950s [7, 8]. However, the early work on the space-charge waves related to the accelerator field started in the 1980s [1, 9].

The most important analysis of the space-charge waves is the linear theory based on a one-dimensional cold fluid model [1]. In this theory, with small initial perturbations, momentum and continuity equations are solved. The solutions show that the modulations travel along the beam in the form of waves called space-charge waves and are the superposition of two eigenfunctions. One of them has a phase velocity greater than the main beam velocity, so it is called the fast space-charge wave. The other has a phase velocity smaller than the main beam velocity, so it is called the slow space-charge wave.

Recent experiments were carried out in the charged-particle beam group at the University of Maryland since the early 1990s [10-12]. In 1993 [11], J.G. Wang and D.X. Wang performed a series of experiments using the Maryland Electron Beam Transport facility. In their experiments, space-charge waves were produced at the gridded cathode of the electron gun by creating local perturbations of beam velocity and current. It was the first success in experimentally generating a single localized space-charge wave, i.e., either a fast wave or a slow wave, instead of generating pairs of waves. Analytical solutions, which show the relations between the evolution of the amplitude and polarity of the space-charge waves and the initial perturbation conditions, can be derived from one-dimensional cold fluid equation under the linear perturbations assumptions. The measurement of wave velocity agrees well with the theory. In 1994 [12], further experimental observations of the reflection and transmission of space-charge waves at the ends of bunched beams were achieved. The speeds of the reflected and transmitted waves were measured. Theoretical analysis led to a critical condition for the existence of the reflection in the experiment. However, the detailed reflection process at an eroded beam shoulder and the propagation of transmitted waves on the beam end are not well understood because of the complexity of the highly nonlinear conditions.

In the late 1990's [13-15], a series of experiments were performed to study the space-charge wave dynamics in a resistive-wall channel at University of Maryland. As before, a grid-voltage perturbation generated a localized perturbation to produce space-charge waves. The perturbation currents were measured by current monitors. In order to measure the longitudinal energy width, two generations of electrostatic

energy analyzers were built, and the preliminary measurement of the change in energy spread of space-charge waves resulting from the resistive wall instability were performed with the first generation of energy analyzer. All these experiment showed good agreement with the linear theory of the resistive wall instability. Later on, the growth rate/decay rate of the longitudinal energy width of the space-charge waves were measured with the second generation retarding voltage energy analyzer designed by Dr. Y. Zou in both linear and nonlinear regime. In the linear regime, the experiment result is the same as the previous: the energy width of the slow wave was observed growing, while the energy width of the fast wave decaying. In the nonlinear regime, the decay rate of the energy width associated with the fast wave was more complicated. As the perturbation strength increased, the fast wave was found to grow. In order to confirm this unexpected observation, the resistive wall was replaced by a conducting tube and the other conditions remained the same. In this case, no growth or decay was observed for the fast wave. There is yet no theoretical explaining for these nonlinear phenomena.

Similar investigations have also been conducted in other labs. Some of the most important work was done by D.A. Callahan et al in 1997 [16] in Lawrence Livermore National Laboratory. A RZ particle-in-cell code was setup to simulate the longitudinal wall impedance instability in a heavy-ion fusion driver. The growth rate of the instability was calculated by both theory and simulation. The results showed that the longitudinal wall impedance instability is not a serious threat to the success of heavy-ion driven inertial confinement fusion.

In all the experiments mentioned above, the perturbations were generated by modulating the gridded electron gun. One of the shortcomings of this method is that the combination of the density and energy modulation make it difficult to obtain an initial condition of pure density modulation or pure energy modulation. The most recent experimental work was performed on the University of Maryland Electron Ring (UMER) [17, 18] by a previous graduate student from the UMER group, Y. Huo. In Y. Huo's experiment [19], an ultraviolet laser was used to impinge on the photocathode in order to generate a pure density perturbation. The current profiles were measured in different chambers along the ring and the evolution of the current modulation was observed. The experimental results were compared with simulation results from WARP code and showed good agreement.

1.2 Motivation

It is believed that space-charge effects are very important to the low-energy, high-intensity beams, but not so important to the high-energy beams for which the emittance is more important. However, that is not true for the space charge waves. As an example, in the SNS, which is under construction in Oak Ridge Tennessee, the negative hydrogen beam is accelerated in an RF Linac to a kinetic energy of 1 GeV. 1060 macrobunches from the Linac are then injected into a storage ring via a high-energy beam transport line, the two electrons of the negative hydrogen ions are stripped, and the beam in the storage ring then consists of protons. The storage ring

has many magnets to confine the proton beam into a circular orbit. If initial density modulations are generated in the early part of the Linac, in which the beam is in a space-charge dominated regime, energy modulations can be obtained from the density modulations even though the beams are accelerated to higher energy later. The associated energy dispersion may cause problems when the beams enter the storage ring. Therefore, to study the nature of space-charge waves evolution is very important for today's high-intensity machines. In this thesis, the energy modulations converted from initial current modulations are measured after the electron beams traveled through a long solenoid channel.

Initial experimental studies have been carried out in some experiments, as was mentioned above. However, the low resolution of the energy analyzer has always limited the evaluation of the experimental results.

The UMER is designed as a flexible and well-diagnosed tool for doing experiments on space-charge dominated beams. In order to enhance the diagnostic ability of UMER, a compact energy analyzer with high resolution was designed by Dr. Y. Cui [20-22]. This is the third generation of retarding voltage energy analyzers, which were developed in our group. The energy analyzer was first inserted into a straight beamline channel that includes a long solenoid to observe the energy spread growth due to the Boersch effect [23, 24]. A computer-controlled automated data-acquisition system was also developed, which greatly increased the efficiency and accuracy of the measurements. It is thus very convenient to use this experimental system also to study the evolution of space-charge waves reported in our current work.

In this thesis, the same methods as those experiments in the 1990s were used to generate the initial density modulation. In the experiment, the initial energy modulation can be neglected compared to the density modulation. Therefore, the initial condition can be considered as a pure density modulation. From the linear theory, energy modulation can be generated by the pure density modulation. However, there is yet no detailed experiment report on these phenomena. In our experiment, after traveling a distance of more than two meters, two peaks with opposite polarity were observed in the energy waveform. One corresponds to a fast wave; the other corresponds to a slow wave. By changing the gun working conditions, different initial conditions are achieved so that the relationship between the initial density modulation strength and excited energy modulation strength can be studied. Comparisons of the experimental results with linear theory and the WARP simulation are also reported.

Chapter 2 Theory and Simulation of Space-charge Waves

In this chapter, the basic theory of space-charge waves in space-charge dominated beams is reviewed. In the first section, a simple one-dimension model is analyzed to derive the fast wave and slow wave perturbations due to a small sinusoid initial velocity modulation. Then in the second section, one dimension cold fluid theory is used to analyze a more complex model, an infinitely long cylindrical beam in a conducting pipe. The analysis results in the definition of sound speed, which is the space-charge wave speed in the beam frame. In the third section, the analytical solution of the space-charge wave evolution with an arbitrary localized current and velocity perturbation can also be solved. With this solution, the condition for generating a single fast wave and a single slow wave is achieved. In the last section, a single fast wave and a single slow wave is generated using WARP simulation.

2.1 Single particle dynamics in a sinusoidal density modulation beam

To understand how perturbations of the longitudinal charge density propagate along the beam as space-charge waves, it is very useful to start with a simple, one dimensional, non-relativistic beam model where boundary effects are ignored. In this model, a strictly one-dimensional geometry in which the beam is infinitely large in the transverse direction is assumed.

From basic theory in plasma physics, local charge perturbations in plasma can generate plasma oscillations with plasma frequency $\omega_p = \left[\frac{q^2 n_0}{\epsilon_0 m \gamma_0^3} \right]^{1/2}$ [25]. Where q is the charge of the particle, n_0 is the charge density, ϵ_0 is the permittivity of the free space; γ_0 is lorentz factor; m is the rest mass of the particle. This theory also applies to a charged-particle beam, which can be treated as non-neutral plasma. If $s(t)$ denotes the particle displacement from the equilibrium position in the moving beam frame as a function of time t , the harmonic oscillation equation of $s(t)$ is:

$$\ddot{s} + \omega_p s = 0 \quad (2.1)$$

The general solution of this equation is:

$$s(t) = C_1 e^{i\omega_p t} + C_2 e^{-i\omega_p t} \quad (2.2)$$

Where C_1 and C_2 are complex constants determined by the initial conditions.

At $t=t_0$, a pure sinusoidal velocity modulation is generated in the longitudinal direction with an amplitude of v_1 and a frequency of ω . The initial condition thus can be expressed as:

$$\begin{aligned} s(t_0) &= 0 \\ \dot{s}(t_0) &= v_1 \cos \omega t_0 \end{aligned} \quad (2.3)$$

It yields the solution of the coefficients in equation (2.2); further, the solution of harmonic oscillation equation can be obtained:

$$s(t, t_0) = \frac{v_1}{2i\omega_p} e^{i(\omega - \omega_p)t_0} e^{i\omega_p t} - \frac{v_1}{2i\omega_p} e^{i(\omega + \omega_p)t_0} e^{-i\omega_p t} \quad (2.4)$$

The distance z of travel from the position of $t=t_0$ can be expressed as

$$z = v_0(t - t_0) \quad (2.5)$$

Where v_0 is the unperturbed velocity.

t_0 can be eliminated in the expression (2.4):

$$s(t, t_0) = \frac{v_1}{2i\omega_p} e^{i(\omega t - k_f z)} - \frac{v_1}{2i\omega_p} e^{i(\omega t + k_s z)} \quad (2.6)$$

This solution represents two traveling waves called space-charge waves, one with wave number k_f and the other with wave number k_s . The two wave numbers are given by:

$$\begin{aligned} k_f &= \frac{\omega - \omega_p}{v_0}, \\ k_s &= \frac{\omega + \omega_p}{v_0}, \end{aligned} \quad (2.7)$$

They also satisfy the dispersion relation, which applies for such perturbations in a cold beam:

$$(\omega - kv_0)^2 = \omega_p^2 \quad (2.8)$$

Thus, the phase velocity and group velocity in the lab frame can be shown:

$$\begin{aligned} v_f &= \frac{\omega}{k_f} = \frac{v_0}{1 - (\omega_p / \omega)} \\ v_s &= \frac{\omega}{k_s} = \frac{v_0}{1 + (\omega_p / \omega)} \end{aligned} \quad (2.9)$$

$$v_g = \frac{\partial \omega}{\partial k} = v_0 \quad (2.10)$$

Since, according to equation (2.9), wave phase velocity v_f is greater than the beam velocity, and which is called the fast wave. The wave phase velocity v_s is smaller than the beam velocity, and called the slow wave. However, equation (2.10) shows that the energy will travel at the velocity of the beam. The same result can be derived if an initial density perturbation is given with the analysis above.

2.2 Analysis of Space-charge waves using the One Dimensional Fluid

Model

The analysis in the previous section is focused on a single particle in the electron beam; the concept of space charge wave can be introduced with this simple model. However, the result is not self consistent, because we neglect the variation of electric field due to the space charge wave. In this section, I will introduce a more complex model to derive a self-consistent result.

In this model, the beam is considered as an infinitely long cylinder of line charge density of Λ and radius a inside a conducting drift tube of radius b . We assume that all the perturbations are much smaller than the DC quantities. Subscripts 0 and 1 represent the unperturbed and perturbed physical quantities respectively. The form of the line charge density, beam velocity and current can be expressed as:

$$\begin{cases} \Lambda(z, t) = \Lambda_0 + \Lambda_1 e^{i(\omega t - kz)} \\ v(z, t) = v_0 + v_1 e^{i(\omega t - kz)} \\ I(z, t) = I_0 + I_1 e^{i(\omega t - kz)} \end{cases} \quad (2.11)$$

Where

$$I = \Lambda v$$

The continuity equation can be expressed as:

$$\frac{\partial(\Lambda v)}{\partial z} + \frac{\partial \Lambda}{\partial t} = 0 \quad (2.12)$$

Substituting (2.10) to (2.11) and (2.12) with the small perturbations assumption, all the terms higher than the first order can be neglected. The final

relationship between the current perturbation and the line charge density perturbation can be linearized in (2.15).

$$I_0 = \Lambda_0 v_0 \quad (2.13)$$

$$I_1 = \Lambda_0 v_1 + v_0 \Lambda_1 \quad (2.14)$$

$$\Lambda_1 = \frac{kI_1}{\omega} \quad (2.15)$$

The longitudinal dynamics equation can be expressed as:

$$\gamma_0^3 m \frac{dv}{dt} = qE_z \quad (2.16)$$

where $\gamma_0^3 m$ is the longitudinal mass; the velocity v can be expressed as equation (2.10), the self electric field due to space-charge can be expressed as:

$$E_z = E_s e^{i(\omega t - kz)} \quad (2.17)$$

One can derive (2.18) from (2.16)

$$v_1 = -i \frac{qE_s}{\gamma_0^3 m(\omega - kv_0)} \quad (2.18)$$

Substituting (2.14) and (2.15) into (2.18), the relationship between the perturbed electric field and the current perturbation amplitude yields:

$$E_s = i \frac{\gamma_0^3 m (\omega - v_0 k)^2}{q\Lambda_0 \omega} I_1 \quad (2.19)$$

The electric field can also be expressed as (2.20) by solving Maxwell's equations:

$$E_s = i \frac{g}{4\pi\epsilon_0} \left(\frac{\partial \Lambda}{\partial z} + \frac{1}{c^2} \frac{\partial I}{\partial t} \right) \quad (2.20)$$

The geometry factor g for space-charge dominated beam is given by:

$$g = 2 \ln \frac{b}{a} \quad (2.21)$$

Therefore, the right hand sides of the equation (2.19) and (2.20) will be equal. Substitution of the expression (2.10) and keeping only the first order term yields the dispersion equation:

$$(\omega - kv_0)^2 - \gamma_0^2 c_s^2 k^2 \left(1 - \frac{\omega^2}{k^2 c^2}\right) = 0 \quad (2.22)$$

The sound speed of the space-charge wave is defined as:

$$c_s = \sqrt{\frac{qg\Lambda_0}{4\pi\epsilon_0\gamma_0^5 m}} \quad (2.23)$$

Under the linear perturbation assumption, the difference between the phase velocities of the two space-charge waves and the beam velocity is very small. Hence, we can make the approximation $\omega = kv_0$, and equation (2.22) can be simplified as:

$$\omega = k(v_0 \pm c_s) \quad (2.24)$$

Thus the phase velocities of the two space-charge waves can be obtained:

$$\begin{aligned} v_f &= v_0 + c_s \\ v_s &= v_0 - c_s \end{aligned} \quad (2.25)$$

Equation (2.25) shows that an observer moving with the beam velocity can see the two space-charge wave moving in opposite directions with the same speed. It is interesting to compare equation (2.8) and (2.25). The difference is due to screening by the wall of the vacuum tube in the second case [1].

2.3 Analytical condition for generating pure slow wave or fast wave

In order to study the evolution of the space-charge waves, a special initial condition is used in this section to solve the one-dimensional cold fluid equation. With the solution, the condition for generating a single fast wave or slow wave can be obtained.

The continuity equation and the momentum transfer equation can be linearized as:

$$\begin{aligned} \frac{\partial \Lambda_1}{\partial t} + v_0 \frac{\partial v_1}{\partial z} + \Lambda_0 \frac{\partial v_1}{\partial z} &= 0 \\ \frac{\partial v_1}{\partial t} + v_0 \frac{\partial v_1}{\partial z} &\approx \frac{e}{m\gamma^3} E_z = \frac{-eg}{4\pi\epsilon_0 m\gamma^5} \frac{\partial \Lambda_1}{\partial z} \end{aligned} \quad (2.26)$$

$$\text{Where } \begin{cases} \Lambda(z, t) = \Lambda_0(z, t) + \Lambda_1(z, t) \\ v(z, t) = v_0(z, t) + v_1(z, t) \\ I(z, t) = I_0(z, t) + I_1(z, t) \end{cases} \quad (2.27)$$

Further more, the initial conditions and boundary conditions are: (a) There is no perturbation anywhere along the z-axis when $t < 0$. (b) At $z=0$ for $t > 0+$ a localized velocity perturbation and current perturbation are introduced in the form:

$$v_1(0, t) = \delta v_0 h(t) \quad (2.28)$$

$$I_1(0, t) = \eta I_0 h(t) \quad (2.29)$$

δ is a small, positive quantity to specify the strength of the velocity perturbation. η is a small quantity to specify the strength of the initial current perturbation and can be negative if the velocity increase causes a current decrease. $h(t)$ is any smooth function with an amplitude of unity which represent the shape of the perturbation and is supposed to vanish when t is equal or smaller than zero. Thus, the line charge density perturbation can be expressed as:

$$\Lambda_1(0, t) = (\eta - \delta)\Lambda_0 h(t) \quad (2.30)$$

By applying the double Laplace transformations for both z and t , the equation (2.26) can be converted to algebraic equations for v_l , A_l and I_l in the k - s domain. Then the algebraic equation can be solved. By applying inverse Laplace transformations, the perturbed beam density, velocity and current in the real time-space domain can be obtained as:

$$\begin{aligned} \Lambda_1(z, t) = & -\frac{\Lambda_0}{2} \left[\delta \frac{v_0}{c_s} - (\eta - \delta) \right] h\left(t - \frac{z}{v_0 - c_s}\right) \\ & + \frac{\Lambda_0}{2} \left[\delta \frac{v_0}{c_s} + (\eta - \delta) \right] h\left(t - \frac{z}{v_0 + c_s}\right) \end{aligned} \quad (2.31 \text{ a})$$

$$\begin{aligned} v_1(z, t) = & \frac{v_0}{2} \left[\delta - (\eta - \delta) \frac{c_s}{v_0} \right] h\left(t - \frac{z}{v_0 - c_s}\right) \\ & + \frac{v_0}{2} \left[\delta + (\eta - \delta) \frac{c_s}{v_0} \right] h\left(t - \frac{z}{v_0 + c_s}\right) \end{aligned} \quad (2.31 \text{ b})$$

$$\begin{aligned} I_1(z, t) = & -\frac{I_0}{2} \left[\delta \frac{v_0}{c_s} - \eta + (\eta - \delta) \frac{c_s}{v_0} \right] h\left(t - \frac{z}{v_0 - c_s}\right) \\ & + \frac{I_0}{2} \left[\delta \frac{v_0}{c_s} + \eta + (\eta - \delta) \frac{c_s}{v_0} \right] h\left(t - \frac{z}{v_0 + c_s}\right) \end{aligned} \quad (2.31 \text{ c})$$

All these expressions have two terms: the first term is the slow wave; the second term is the fast wave. Both the fast wave and the slow wave keep the shape of the initial perturbation, while the amplitude and polarity are decided by the initial conditions.

It is very easy to see that the condition for generating only fast wave is:

$$\frac{\eta}{\delta} = 1 + \frac{v_0}{c_s} \quad (2.32)$$

The condition for generating only slow wave is:

$$\frac{\eta}{\delta} = 1 - \frac{v_0}{c_s} \quad (2.33)$$

2.4 Generation of pure fast or slow wave perturbation in WARP

Simulations

In this section, simulations [27] using WARP are performed to verify the theoretical prediction in equation (2.32) and (2.33). The Warp simulation code was developed to study high current ion beams [26]. It was developed originally to aid in the pursuit of heavy-ion driven inertial confinement fusion (HIF). The Warp code contains a hierarchy of models. The principal models are the PIC models with differing dimensionality. The Warp3D part of the Warp is a three-dimensional model. Other models include WarpRZ, which is an axisymmetric model, and WarpXY. WARP also contains an envelope equation solver, as well as two models that couple a transverse envelope solution with a longitudinal fluid model. In this section, the R-Z geometry in Warp3D part is used to simulate the space-charge wave evolution.

A group of typical beam parameters in the linear transportation experiment at UMER lab is used in the WARP code. These include: beam pulse length is set as 100 ns; main beam kinetic energy $E_0=5090$ eV; unperturbed beam current $I_0=100$ mA; beam radius $a=0.5$ cm; beam pipe radius $b=0.75$ inch. Therefore, more parameters for the beam can be calculated: main beam velocity $v_0=4.2314 \times 10^7$ m/s; generalized perveance $K=0.004049$; the sound speed of space-charge wave $c_s=3.083 \times 10^6$ m/s. So, from equation (2.31) and (2.32), the condition for generating fast wave only is $\eta/\delta=14.725$; the condition for generating slow wave only is $\eta/\delta=-12.725$.

In order to generate a single fast wave in WARP, an initial current perturbation with a strength $\eta=0.04417$ and an initial velocity perturbation with a strength $\delta=0.003$ are loaded to the beam. Both of these perturbations are 20 ns wide and located at the beam center with a Gaussian shape.

Another simulation is performed to generate a single slow wave in WARP. The location, shape and width of the perturbations are the same as in the case for generating a single fast wave. While, the initial current perturbation strength is $\eta=-0.03817$; the initial velocity perturbation has a strength $\delta=0.003$.

For both cases, a uniform focusing channel is loaded to match the 100 mA beam. Other numerical settings for these two cases in WARP are: number of cells in R direction is 128; number of cells in z direction is 256; number of macro particles is 500000.

The simulation results for these two cases are shown in Figure 2.1 to Figure 2.4. All the pictures are taken at $z=0, 0.9, 1.8, 3.6, 5.4$ and 6 meters respectively. Figure 2.1 and Figure 2.3 show the beam current evolution in the beam frame; Figure 2.2 and Figure 2.4 show the beam velocity evolution in the rest lab frame. One can observe a single positive perturbation move toward the beam head in both Figure 2.1 and 2.2, which are corresponding to fast waves. Similarly, a negative slow wave for current perturbation and a positive slow wave for velocity perturbation can be observed moving toward the beam end in Figure 2.3 and 2.4 respectively. The vertical lines in all the figures show the approximate position of beam center. These results show good agreement with the one cold fluid theory prediction in previous section.

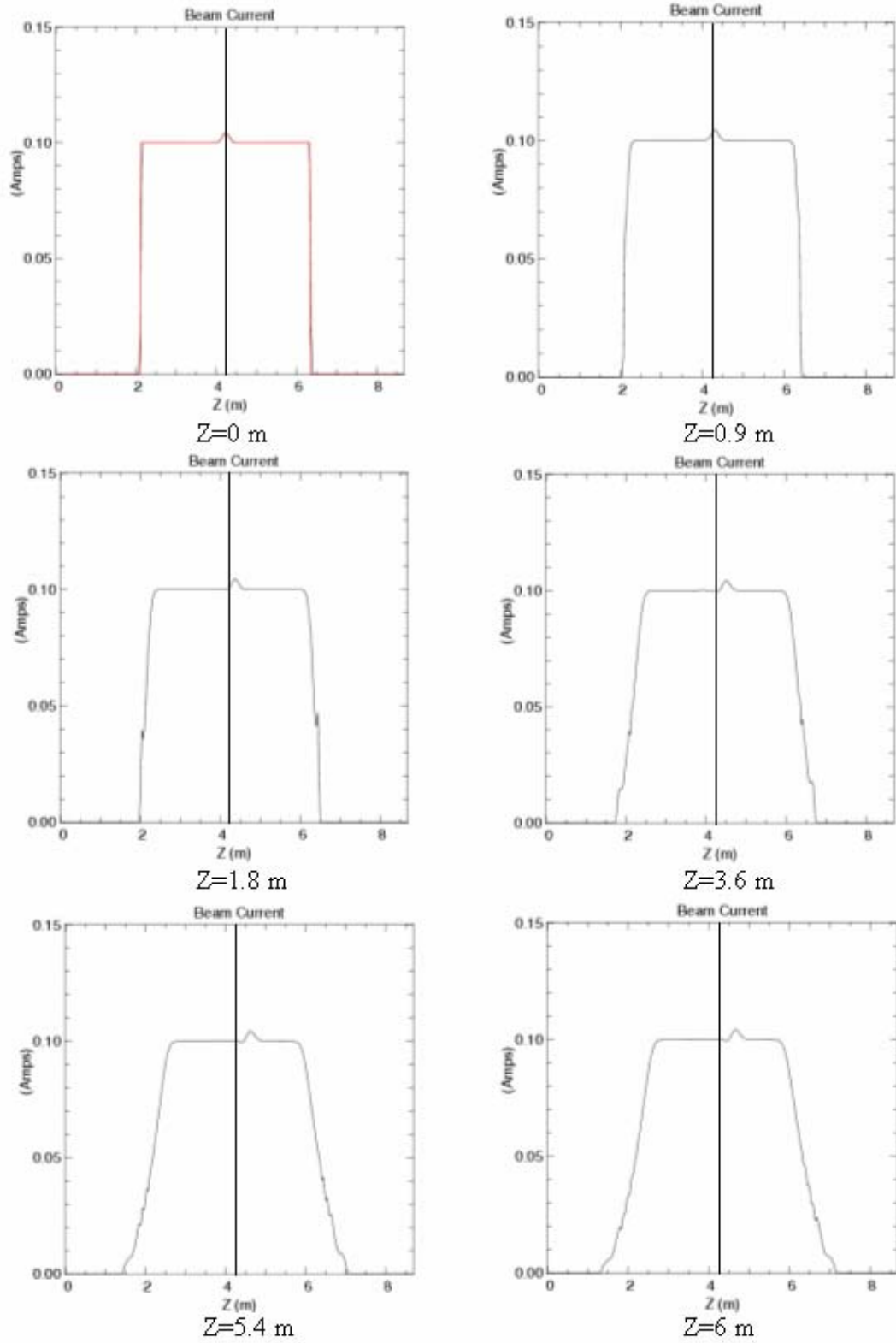


Figure 2.1 current perturbation evolution in WARP with $\delta=0.003$ $\eta=0.04417$

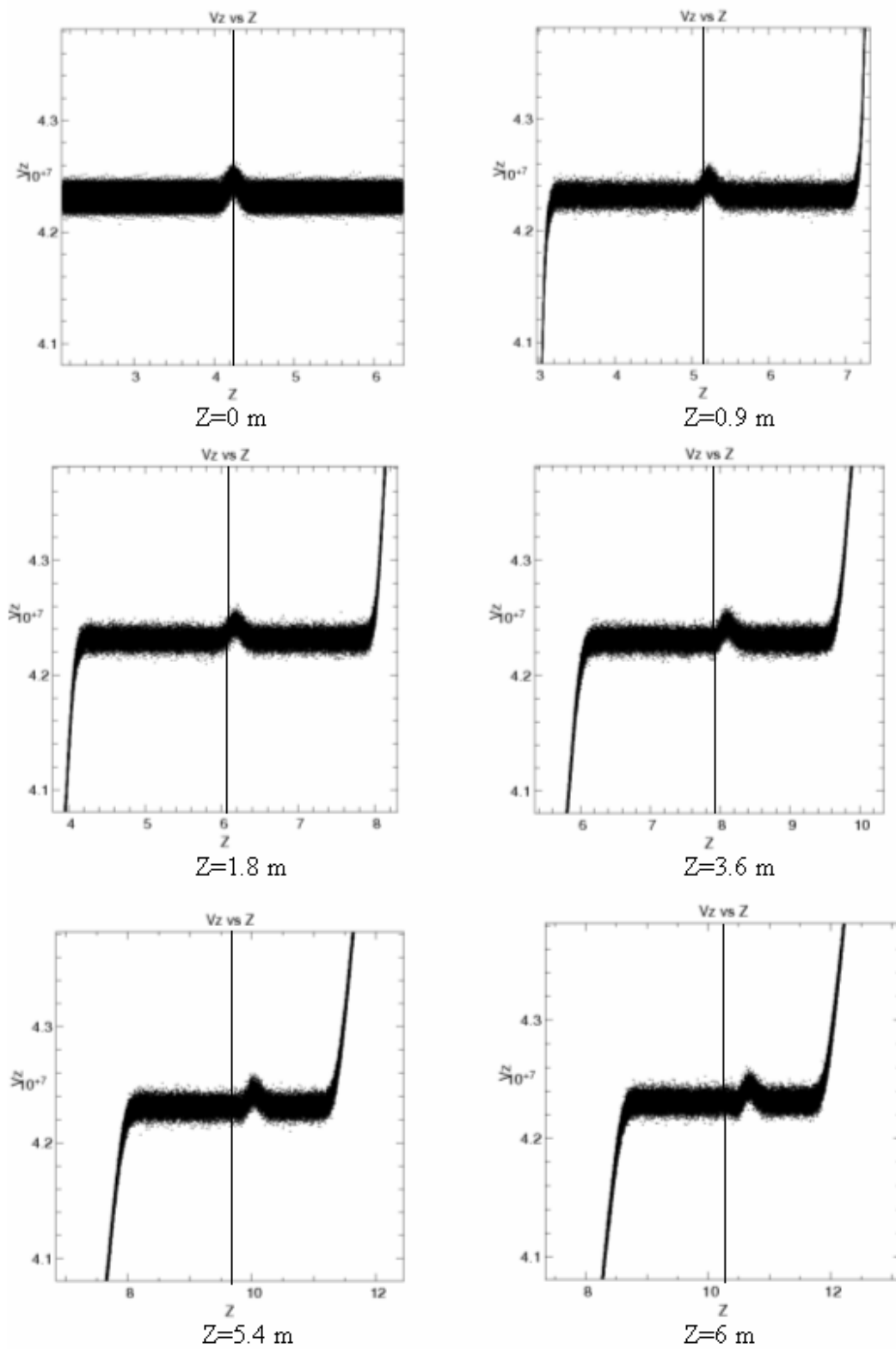


Figure 2.2 Velocity perturbation evolution in WARP with $\delta=0.003$ $\eta=0.04417$

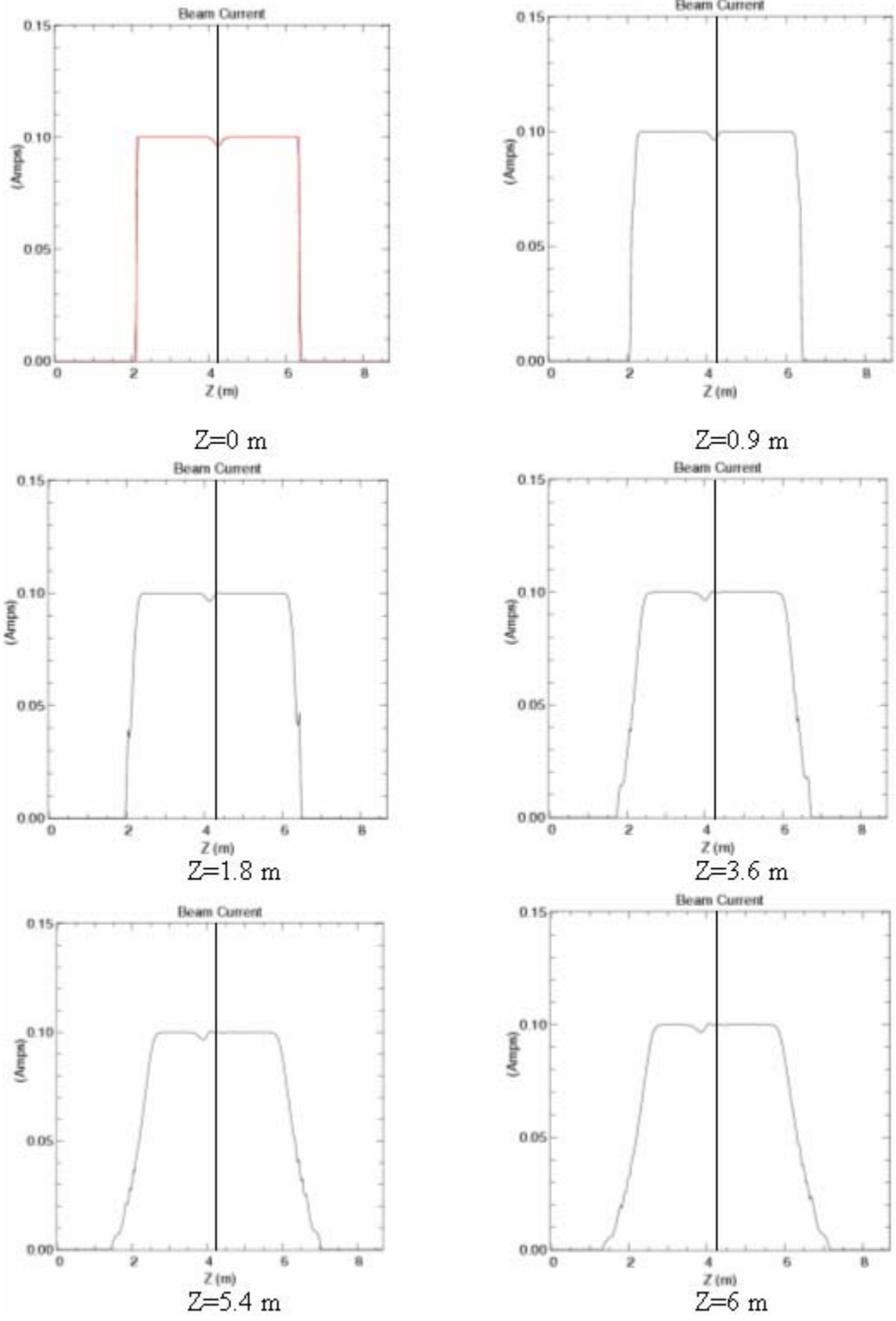


Figure 2.3 Current perturbation evolution in WARP with $\delta=0.003$ $\eta=-0.03817$

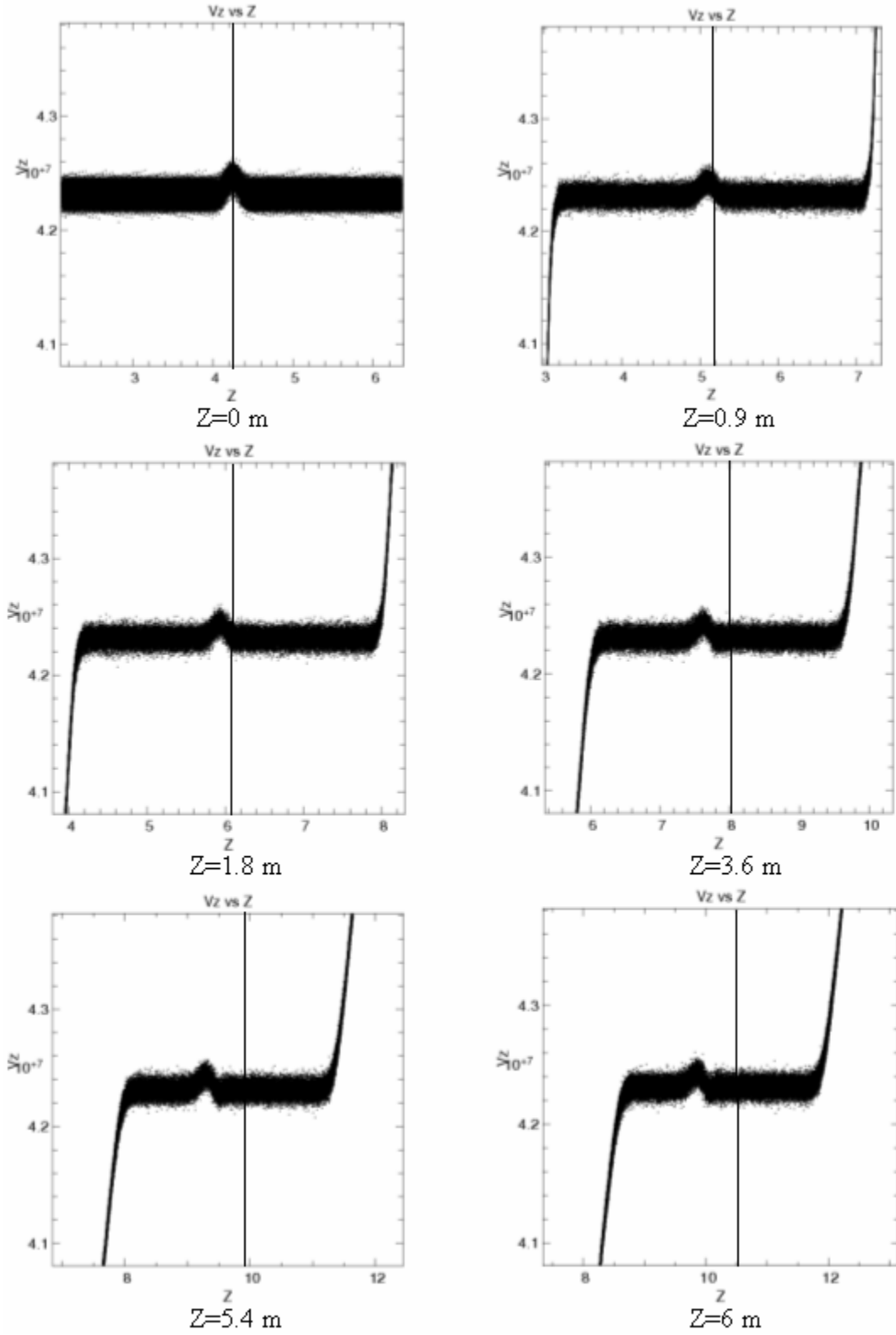


Figure 2.4 velocity perturbation evolution in WARP with $\delta=0.003$ $\eta=-0.03817$

Chapter 3 Experiment study on the space-charge wave evolution

In this chapter, I will report the experimental study on space-charge wave evolution in a uniform focusing channel. The experiment setup is introduced first, which includes the description of the whole system, gun electronics, the energy analyzer and the solenoid. The experiment is performed to generate localized pure current perturbations with different strengths by modulating grid-voltage at the electron gun. The kinetic energy of the beam is measured after the long solenoid. As theoretical prediction, the space-charge waves of kinetic energy appear in pairs, one is fast wave with a positive polarity, and the other is slow wave with a negative polarity. Then the initial current waveforms are imported to the WARP code and simulations are performed to compare the results with the experiment. The experiment and simulation results are also compared with the analytical solution from one-dimensional theory.

3.1 Experimental setup for the study of the space-charge wave

3.1.1 Introduction

A 2.3 m long beam transport line was set up at the University of Maryland to study the longitudinal space-charge perturbation and energy spread evolution in a long uniform focusing channel. The schematic [28] of the whole system is shown in the figure 3.1. A thermionic triode gun is used as the electron beams source. A high-resolution energy analyzer is installed in the system. The long solenoid M4, which is 1.4 meter long, serves as a uniform focusing channel to transport the beam into the energy analyzer. In order to match the beam into the long solenoid, three short solenoids, M1, M2 and M3, are placed in the system. Another short solenoid M5 is placed between the exit of the long solenoid and the energy analyzer in order to control the amount of current injected into the energy analyzer. One Bergoz fast current transformer is located between solenoids M3 and M4. A high vacuum is maintained by four ion pumps, with a very high vacuum at low 10^{-8} to high 10^{-9} Torr. The first ion pump is located at the electron gun with a capacity of 8 l/s. The other three ion pumps have capacities of 40 l/s. One is located between the second and third solenoids and two are located at the diagnostic chamber.

The beam pipeline is connected with an automated measurement system including a high-voltage power supply, a Tektronix oscilloscope (TEK DSA 601A) and a computer. A Matlab code “match” is also developed to guide the setting of the currents of the solenoids to match the electron beams into the long solenoid.

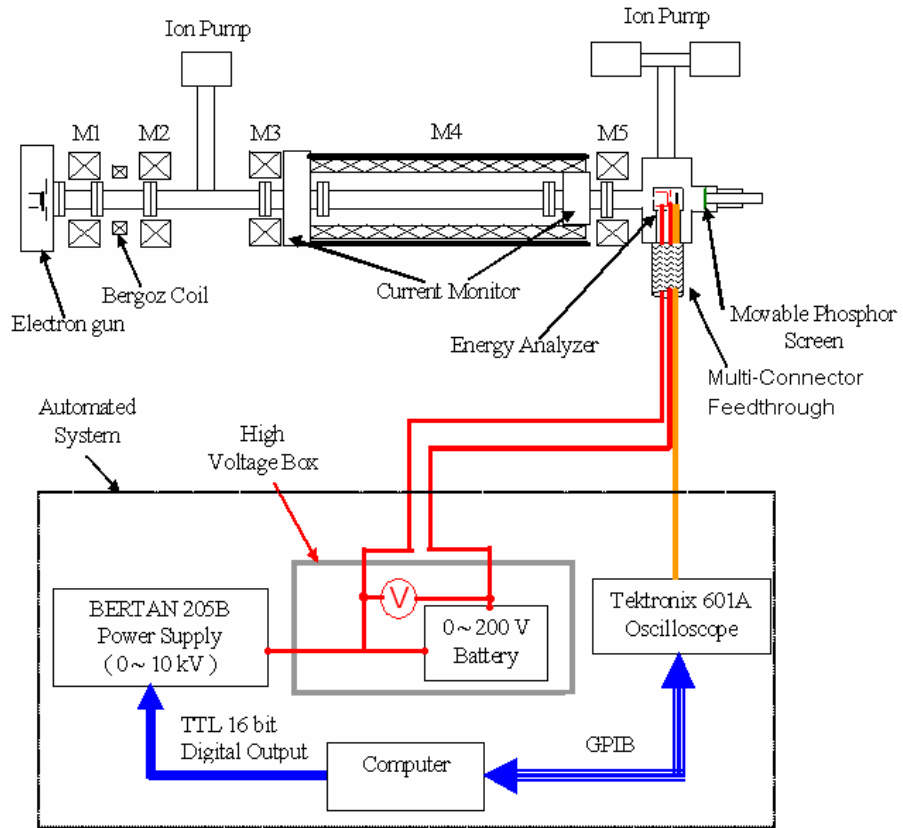


Figure 3.1 schematic of the long transport line experimental setup

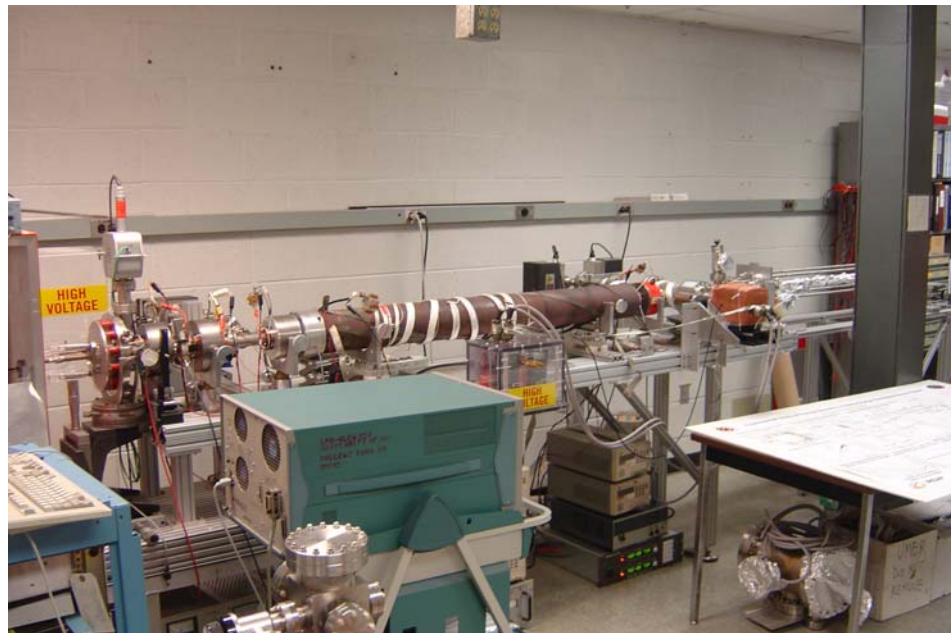


Figure 3.2 Photo of the long transport line experimental setup

3.1.2 Description of the Electron Gun

The electron gun used in the system is a variable-perveance gridded gun developed and constructed at the University of Maryland. The detailed mechanical drawing of the gun can be found in reference [29]. A standard B-type thermionic dispenser cathode, porous tungsten matrix impregnated with barium calcium aluminate ($6\text{BaO}-1\text{CaO}-2\text{Al}_2\text{O}_3$) was used in the gun. The radius of the cathode is 4 mm and the heated area is around 0.5 cm^2 . With such a small heated area, the heating inhomogeneity is not a problem. The anode and the field-shaping electrodes form a Pierce geometry. The distance between the cathode and anode is adjustable by means of micrometers to anywhere between 9.3 mm and 23 mm, allowing us to change the gun perveance. This gun also has a gate valve to isolate the cathode from the rest of the system. The gate valve is only open during experiments, while at other times or during system installation, the gate valve is closed to protect the cathode.

The Circuit diagram for the electron gun is shown in Figure 3.3. The gun electronics consist of a high-voltage supply for the anode grid, an AC power supply for the cathode heater, a DC cathode-grid bias supply (30 V to suppress the beam), and a grid-cathode pulser which provides a fast pulse signal between the cathode and grid to create the beam pulse. This pulse is triggered by an external triggering circuit. Figure 3.3 shows the circuit diagram for the electron gun. High voltage is applied to the anode grid through a $1\text{ M}\Omega$ resistor, which protects the high-voltage power supply from damage in the event of a large discharge when the power supply turns off. All the electronics are located in a high-voltage deck, which is isolated from the ground

and charged up to -10 kV, except for the external triggering circuit, which is at the low voltage and is connected to the high-voltage electronics by fiber optics and an insulated transformer. The cathode is biased by positive DC voltage (30 V) relative to the grid to cut off the beam current. During emission, the grid-cathode pulse generator produces a negative pulse (-60 V) between the cathode and the grid to turn on the beam. The pulse signal is formed with a transmission line and the length of the transmission line, which is variable, determining the beam pulse width. In this experiment, we use a length of the transmission line of about 10 m to produce a 100 ns beam pulse. When the DC charging voltage is below -130 V (in the experiment, it is -160 V), the transistor works in the avalanche state. The avalanche transistor is turned on with the external triggering circuit. A typical grid-cathode pulse signal is below -60 V with a rise time of 2 ns, running at 60 Hz.

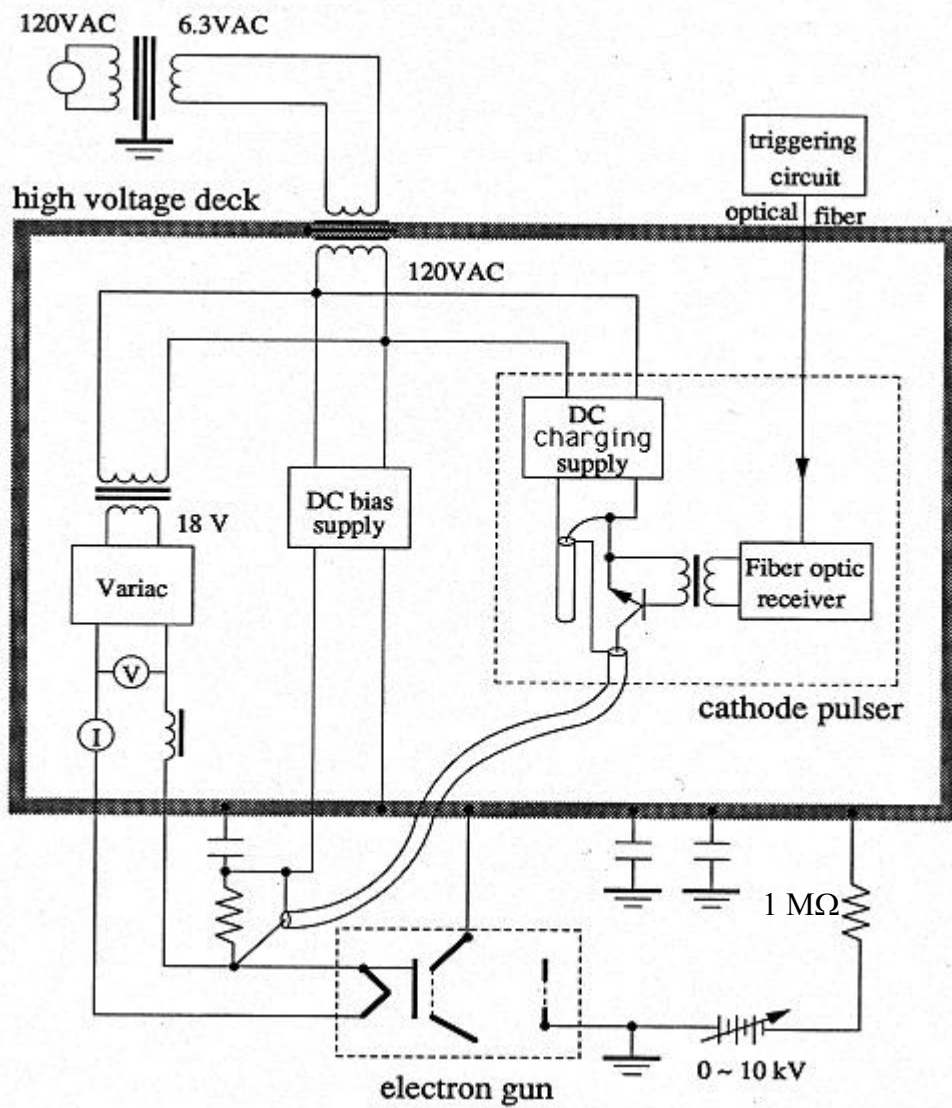


Figure 3.3 Circuit diagram for the electron gun

3.1.3 Energy Analyzer

At University of Maryland, efforts on the development of the high resolution retarding energy analyzer have been made during the past years. In the current system, a third generation energy analyzer is located in the diagnostic chamber after 4 short solenoids and a long solenoid. The mechanical schematic and electrical circuit of this energy analyzer is shown in the figure 3.4. The third generation energy analyzer is a compact device with a length of 4.8 cm and a diameter of 5.1 cm. Thus it is convenient to insert the device into the beam line. A grounded steel plate with a 1 mm diameter circular aperture can let a small amount of beam pass into the high potential region. The high-voltage steel cylinder with a length of 2.5 cm and an inner diameter of 2.5 cm serve as a radial focusing electrode in the energy analyzer. The retarding grid is a molybdenum wire mesh with a transmission rate of 80% mounted on a machinable ceramic (MACOR) ring, which insulates the retarding grid from the focusing cylinder so that the battery inside a external box can supply a voltage difference between the focusing cylinder and the retarding mesh. Both of them are connected to the same external high-voltage source through different high voltage input pins. Behind the high-voltage mesh there is a copper collector plate, from which the current signal is picked up by a 50 Ω BNC connector.

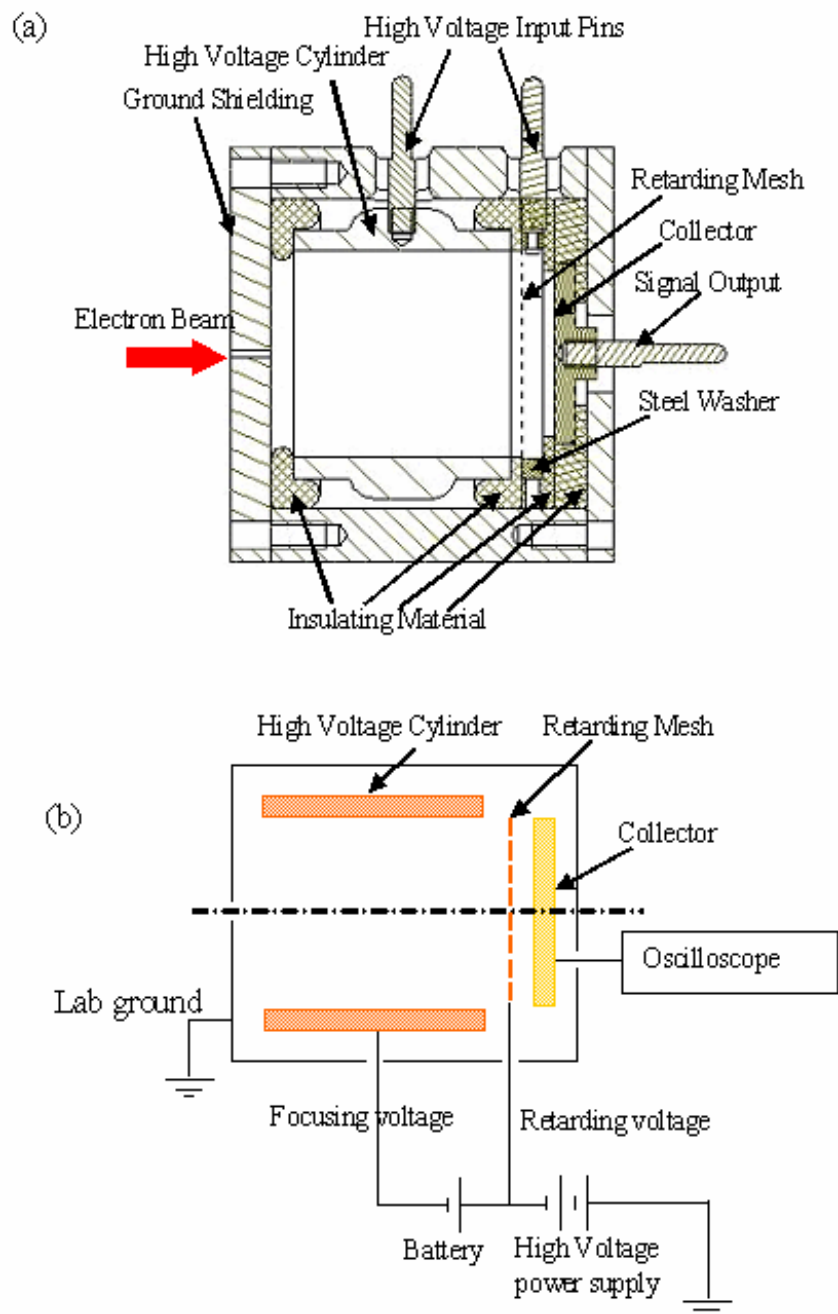


Figure 3.4 (a) mechanical schematic of the energy analyzer (b) electrical circuit of this energy analyzer

The connection of the energy analyzer in the experiment system can be shown in Figure 3.1. The high-voltage power supply used to retard the beam is Bertan 205B, which has low noise and high resolution, with maximum output voltage of 10 kV. The output high voltage of the power supply can be controlled locally via a precision front panel or can be remotely programmed by a 16-bit digital signal. A battery provides the voltage on the focusing cylinder of the energy analyzer, which is in series with the high-voltage output from the power supply. The energy analyzer output current signal is sent directly to the oscilloscope. To improve the experimental efficiency and resolution, Dr. Cui developed a computer-controlled automated data-acquisition system. The entire control program is written in C language for high efficiency and low-level controllability. With this system, we can set the scanning retarding voltage region and voltage step, select signal channel from the oscilloscope, set filter on/off, average number, etc. A full set of data can be taken within several minutes, which is impossible with manual control, as the way people did before. The data taken by the computer are then automatically processed by a Matlab code, which can analyze the data and display detailed information about the beam energy spread within a couple of seconds. The data-processing software can provide time-resolved root-mean-square (rms) energy spread, full width at half-maximum (FWHM), peak, and mean energy along the beam pulse.

3.1.4 Solenoids

As mentioned above, there are 4 short solenoids and 1 long solenoid in the system. The current of each of them can be adjusted individually by different DC power supplies. All the solenoids were re-characterized for this experiment. The fields were measured by a Bell gaussmeter with a longitudinal Hall probe. The distance between the solenoid center and aperture of gun is shown in the table 3.1.

Table 3.1 Data for the solenoids

Solenoid	M1	M2	M3	M4	M5
Solenoid Center to Aperture of gun (cm)	11	27	51.6	133.5	210
Effective Length (cm)	4.34	4.24	7.28	130.8	5.16

The short solenoids each have the same inner diameters of 7.6 cm. the long solenoid M4 is 138.7 cm long. It is made of copper windings on an aluminum tube with a diameter of 11.5 cm. There is an iron tube on the outside of the copper windings to restrict the field lines. The axial magnetic field is uniform inside the solenoid. However, at the edges, the fields decay with distance. The effective lengths of the four short solenoids and the long solenoid are also shown in table 3.1.

3.2 Experimental study on the localized density modulation evolution

3.2.1 Generation of a localized pure current perturbation at the gun

The basic idea of this experiment is to observe the energy perturbation which is excited by a pure current perturbation. In order to produce a pure current modulation at the electron gun, a cable is connected to the middle of the pulse generation transmission line through a “T” connector. As a result, a perturbation is generated at the center of the voltage pulse, which can introduce a perturbation to the beam current. The nominal beam energies in all the experiment are 5 Kev, while the perturbation of the voltage is very small compared to this value, so in most case, the energy modulation created by the voltage pulse can be neglected. According to the theoretical predictions, both current and velocity perturbations will exist in the form of a fast wave and a slow wave at the downstream of the transport line. The energy perturbation waveform can be measured by the Energy analyzer after the long solenoid. The current perturbation can be measured using the Bergoz current monitor.

In order to generate different current perturbation strength, we change the bias voltage of the electron gun. One should notice that the main beam currents are also changed with this method. Four groups of electron beams with different nominal current and different current perturbation strengths are achieved, as shown in Table 3.2. The current profiles shown in the Figure 3.5 are acquired from the Bergoz current monitor between matching solenoid M2 and M3.

Table 3.2 Data for current perturbation generation at the gun

Group #.	Bias Voltage V	Main current mA	Current Perturbation/mA	Perturbation strength/ η
1	2	69.6	3.97	0.057
2	14	77.4	10.85	0.137
3	30	67.2	16.00	0.226
4	32	45.6	13.20	0.29

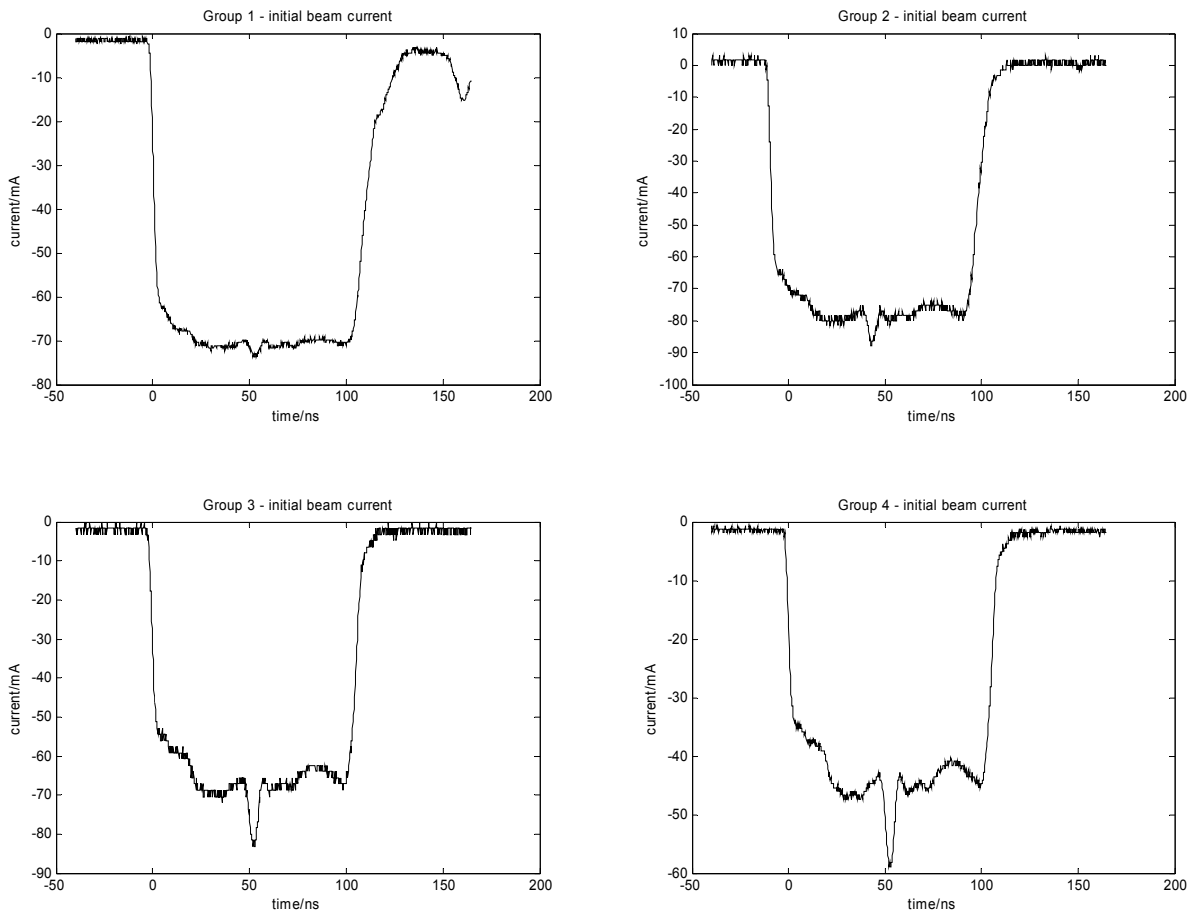


Figure 3.5 Four groups of initial currents with perturbation

3.2.2 Measurement of energy perturbation with energy analyzer

If we change the regarding voltage, a series of current signal are acquired by the energy analyzer. With this data, the relation between the current signal and the retarding voltage for a specific location at the beam can be plotted as a curve. The differentiation of this curve results in the energy spectrum for this special point of the beam. To illustrate this procedure, we take Group 3 as an example. During the experiment, the retarding voltage is scanned automatically from 4930 Volts to 5180 Volts by a step of 2 Volts. That means, every 2 volts, a current signal is taken by the automation measurement system and the data is stored in the computer. Figure 3.6 shows some of these current profiles. With this data, the relation between the current and the retarding voltage can be obtained for any position of the beam. In Figure 3.7(a), the red curve represent the current versus retarding voltage for $t=58\text{ns}$. The blue curve, the energy spectrum at $t=58\text{ ns}$, is derived by differentiating the red curve.

In Figure 3.7(a), some abnormal jumps of data in the red curve are observed. These jumps can introduce erroneous peaks into the energy spectrum curve. Obviously, these individual jumps are due to some measurement error. In order to reduce the error, an algorithm to smooth the data locally is used. After finding a jump, if its relative value to the biggest jump is larger than the threshold value, the data around that jump in a specific range will be smoothed. Figure 3.7(b) shows the result after smoothing.

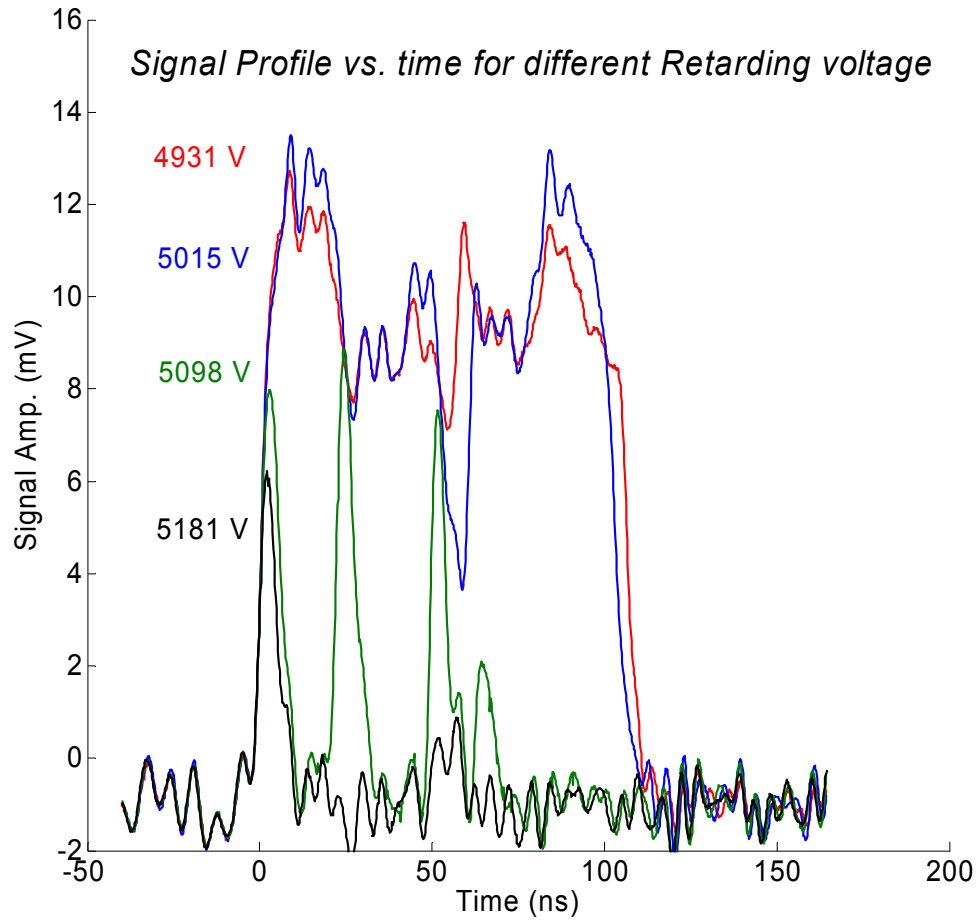
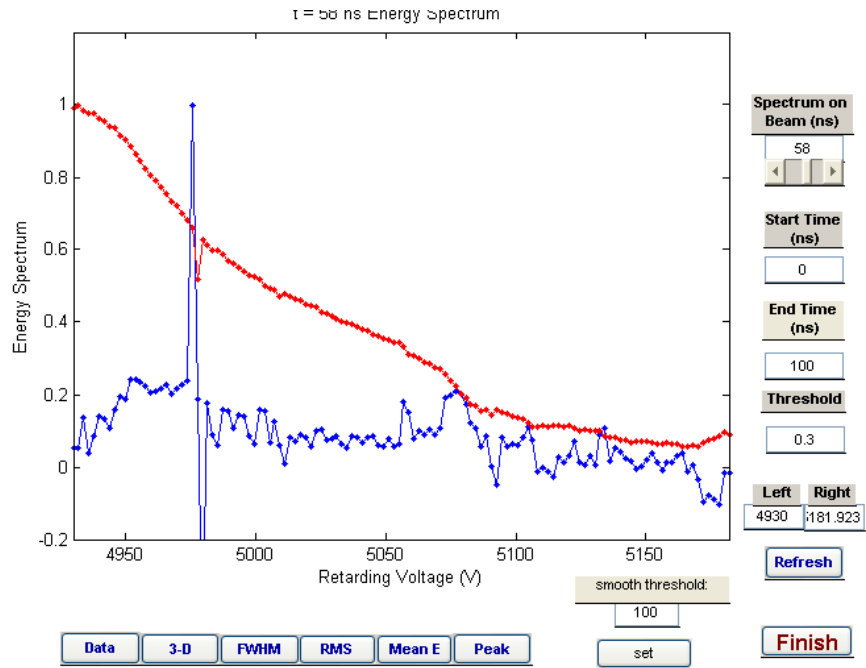
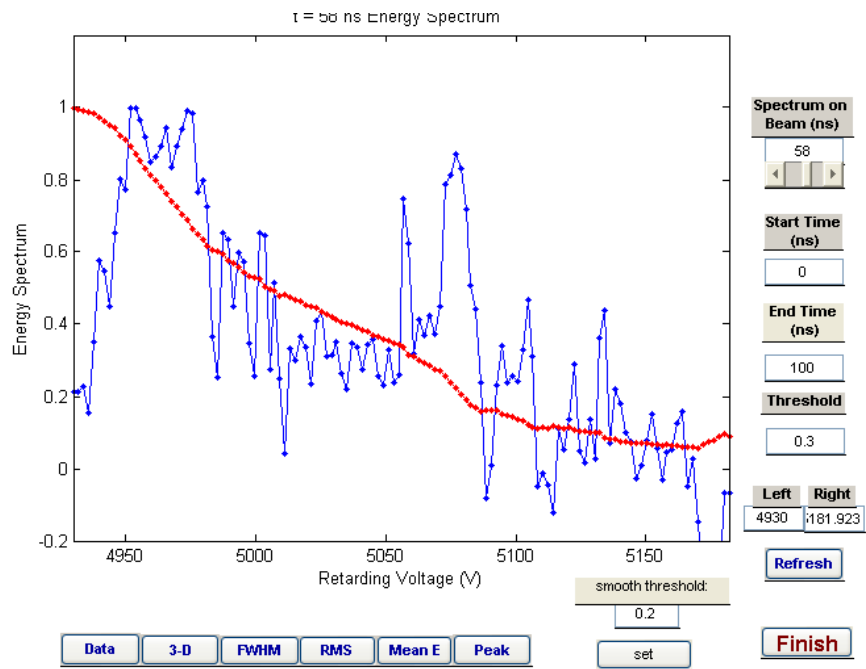


Figure 3.6 Current signals acquired by energy analyzer with different retarding voltage in Group 3



(a)



(b)

Figure 3.7 (a) the red curve represent the current versus retarding voltage and the blue curve is the energy spectrum before smoothing (b) data after smoothing

With the energy spectrum at different positions in the beam, the mean energy along the beam can be calculated easily by integrating the energy spectrum. In figure 3.8, we plot the mean energy along the beam at 2.3 meters before the gun. As the theory predicts, with the initial condition of pure density modulation, energy modulation can be achieved. The energy modulation splits into two peaks at the beam center: one is positive and near to the beam head, which corresponds to the fast wave, the other is a negative peak and near to the beam end, which corresponds to the slow wave. According to the one-dimensional cold fluid theory, the peaks of fast wave and slow wave should have the same amplitude. However, here we see some inconsistency with the theoretical predictions. Especially for the result of group 4, the amplitude of slow wave is much bigger than that of fast wave. The reason for this is not clear up to now. However, it may be related to the following two aspects: First, for group 3 and group 4, the current perturbations are more than 20% of the main beam current, so the nonlinear effect should not be neglected, while the one dimension theory has the assumption of linear conditions. Second, during the experiment, the beams are not stable enough, which also brings errors to the measurement. Another observation is that some other peaks are obtained for these four groups of results. Compared with the initial currents in Figure 3.5, it is not difficult to find that they are due to the bumps near the beam head and beam end. However, we do not need to worry too much about these peaks. We may want to focus more on the peaks for the slow wave and fast wave at the beam center.

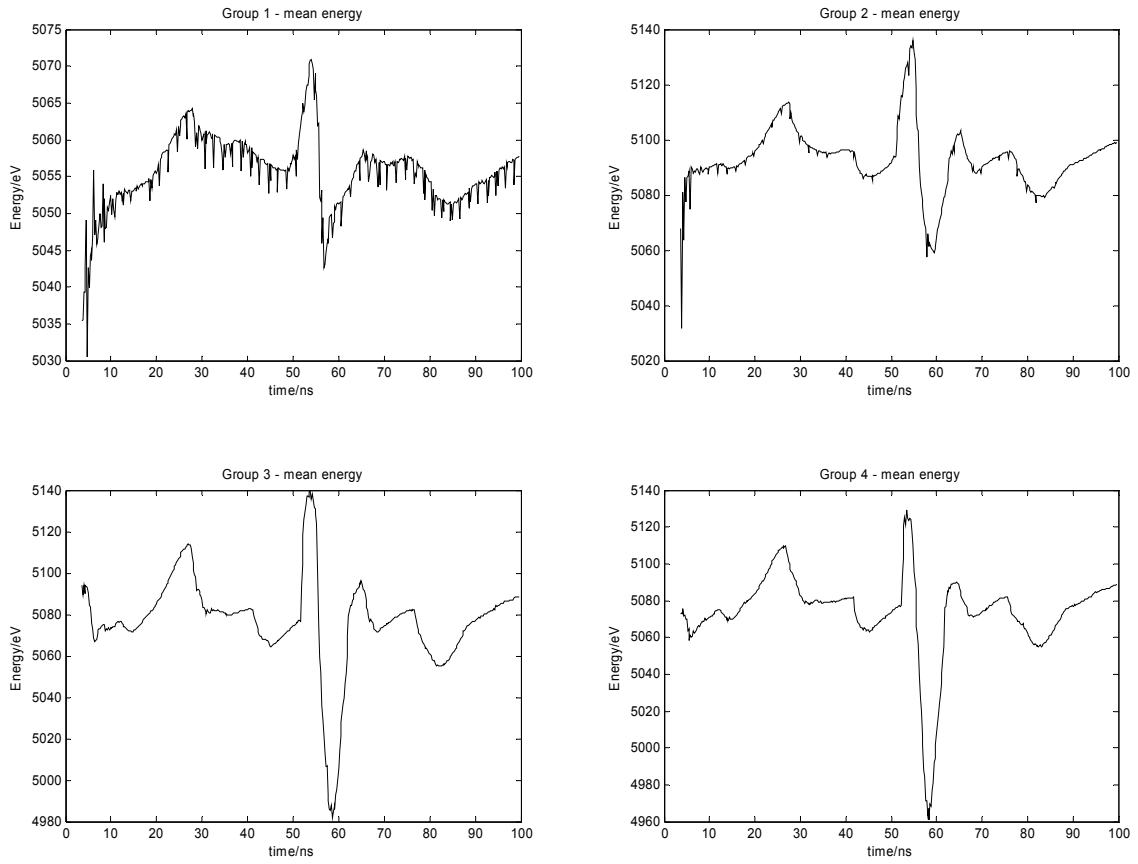


Figure 3.8 Mean energy waveforms derived from energy analyzer signals for different groups

3.3 Experiment result analysis and comparison with theory and simulation

In this section, the experimental results for the energy perturbation are analyzed quantitatively. The peak-to-peak values for the energy perturbation are calculated for each group; then the relationship between these values and the initial current perturbation strength is studied. The same analysis can also be performed using WARP simulation and the linear evolution theory derived from the one-dimensional cold fluid theory. The comparisons among the experiment results, simulation results and theory prediction will also be given.

3.3.1 Import the beam current into WARP

With the automated data acquisition system, the current profile measured by Bergoz coil can be acquired and will be stored by computer, so it is very convenient to import the values of the beam in the experiment generated by the electron gun into the WARP code. Then use WARP code to simulate the beam propagation. So, the introduction of the initial setup in WARP will be presented first.

First, the current profiles of the Bergoz coil are imported into the WARP code to serve as the initial current of the simulation. Here the data of group 3 are taken as an example, which is shown as the red curve the in Figure 3.9. Lots of noise are observed in the current profiles. In order to reduce the noise, data is smoothed before the simulation in WARP starts. The black curve in Figure 3.9 is the current after the

smoothing procedure. The energy perturbation is set zero initially. The current profiles are measured by the Bergoz current monitor, which is about 15 cm before the cathode, so there should be some initial velocity perturbations initially. The initial energy setting in WARP may introduce some errors.

Then, the parameters such as beam radius R , main beam current I_0 and main beam kinetic energy E_0 are set up in the WARP code. Beam radius is calculated from envelope equation using the long solenoid strength data from experiment. Different settings for each group are shown in table 3.4. After that, a uniform focusing channel is set up to transport the beam. The strength of the focusing channel is calculated by the envelope solver of WARP based on the initial setting of beam parameters. Other settings for numerical simulation are: beam length is 100 ns; particle number is 50000; the number of cell in r direction is 64; the number of cell in z direction is 256.

Next, the simulations are carried out in the R - Z geometry for 2.3 meters, which is the distance between the Bergoz coil and the retarding field energy analyzer in experiment.

Table 3.3 Beam parameters setting in WARP

Group number	I_0 /mA	E_0 /eV	R /mm
1	69.6	5055	5.3
2	79.2	5092	5.6
3	67.2	5074	5.2
4	45.6	5077	4.4

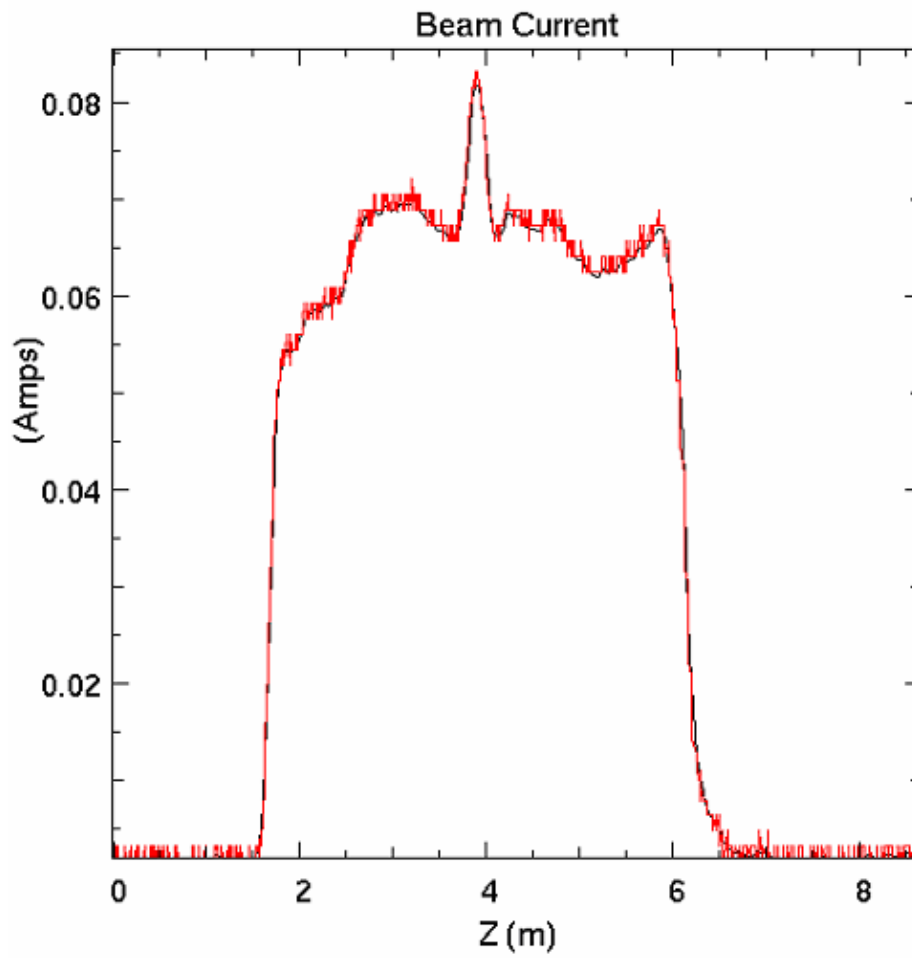


Figure 3.9 Current profile imported into WARP in Group 3

3.3.2 Comparison of the wave shapes for the mean energy along the beam

With the initial settings in the last section, WARP-RZ code can solve the propagation of the wave in the uniform focusing channel, thus giving velocity distribution after the beam transport for 2.3 meters. On the other hand, based on the one dimension cold fluid theory, if we know the initial perturbation velocity perturbation strength is 0, the evolution of the velocity space-charge wave can be simplified from equation (2.31):

$$\Lambda_1(z, t) = \frac{\Lambda_0 \eta}{2} h\left(t - \frac{z}{v_0 - c_s}\right) + \frac{\Lambda_0 \eta}{2} h\left(t - \frac{z}{v_0 + c_s}\right) \quad (3.1a)$$

$$v_1(z, t) = -\frac{\eta c_s}{2} h\left(t - \frac{z}{v_0 - c_s}\right) + \frac{\eta c_s}{2} h\left(t - \frac{z}{v_0 + c_s}\right) \quad (3.1b)$$

$$I_1(z, t) = \frac{I_0 \eta}{2} \left(1 - \frac{c_s}{v_0}\right) h\left(t - \frac{z}{v_0 - c_s}\right) + \frac{I_0 \eta}{2} \left(1 + \frac{c_s}{v_0}\right) h\left(t - \frac{z}{v_0 + c_s}\right) \quad (3.1c)$$

With the initial current perturbation strengths η and the initial current profiles from experiment data, it is very easy to get the analytical solution of these equations for each group. A Matlab code [30] has been developed to perform this theoretical calculation.

The results from WARP and one dimension theory are shown in Figure 3.10 with the experiment results: the WARP results are represented by the red curve; the experiment results are represented by the black curve; the one-dimensional cold fluid theory predictions are represented by the green curve. From these curves, the similar shape of the energy perturbations for WARP simulation, experiment results and the

one-dimensional cold fluid theory can be observed in each group. Except for the fast wave and slow wave generated near the beam center, some other perturbation peaks with positive and negative polarity can be observed near the beam head and beam tail. Compared with the initial current, there are some bumps near the beam head and tail. These bumps may introduce instability in the beam and generate space-charge waves.

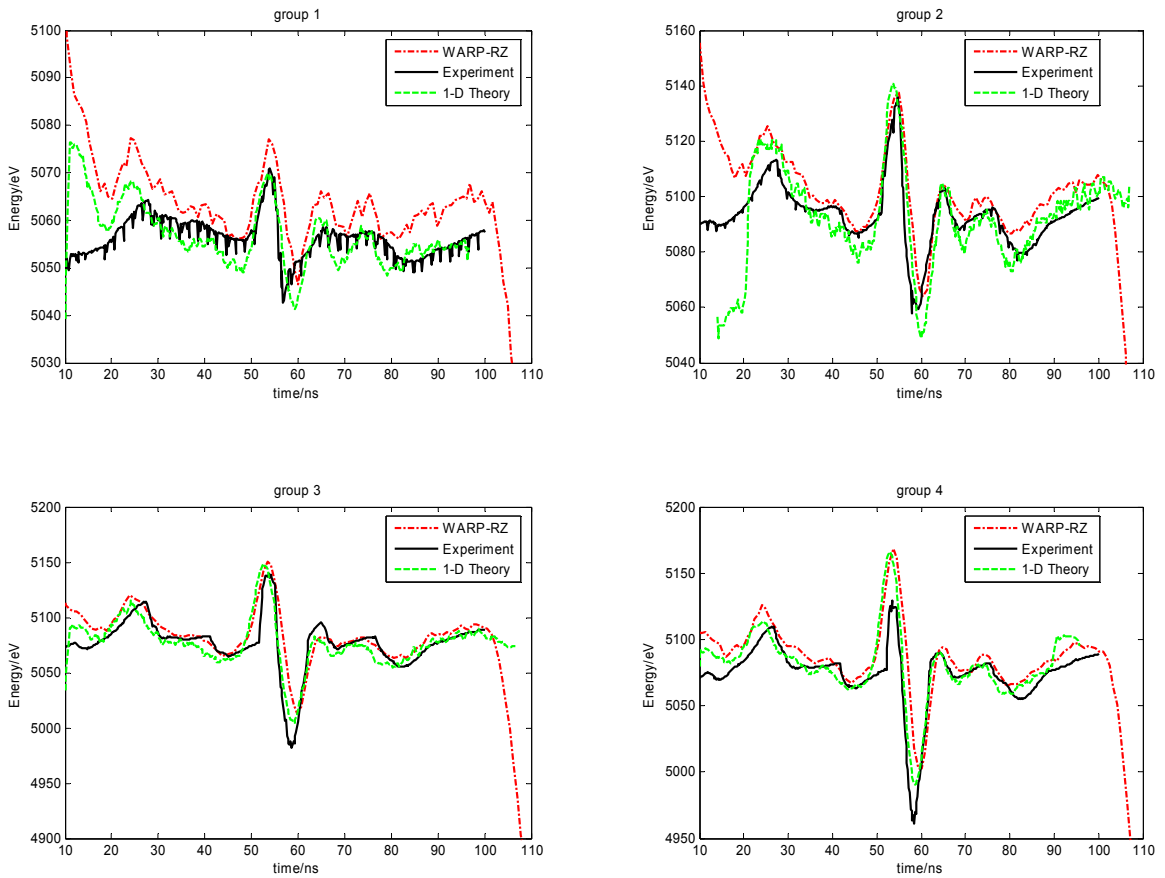


Figure 3.10 Comparisons of the wave form of mean energy for the experiment results, WARP simulation results and one-dimensional cold fluid theory

3.3.3 Relation between the strengths of initial current perturbation and final energy perturbation achieved

One can observe from Figure 3.10 that the amplitudes of the energy perturbations are not equal for different calculation method in each group. In order to compare the deviation among the results from experiment, WARP and one dimensional theory, the values of the energy perturbation peaks are measured. The space-charge waves were transported for only 2.3 meters before they are measured, so the fast wave and slow wave due to the current perturbation at the beam center may not separate completely. This indicates that these peaks can be smaller than those derived after the pair of space-charge wave separate completely. Also, because the main beam current is not flat as ideal beam pulse but has some bumps, which introduce additional current perturbations along the beam other than the perturbation generated at the center of the beam. We cannot observe the complete separation of the slow wave and fast wave even after the beam transport for a longer distance, so that the two waves generated by the current perturbation at the beam center separate completely. Therefore, the perturbations we observed are always the superposition of slow wave and fast wave.

To compare the experiment results with simulation and theory results in quantity, it is useful to compare the peak-to-peak value using a different calculation method, which is defined as the difference between peak value of fast wave and slow wave. The values for the energy perturbation peak-to-peak strengths $\Delta E/E_0$ measured

at $Z=2.3$ meters using different method and initial current perturbation strengths η , their values are shown in table 3.5.

Table 3.4 Energy perturbation peak-to-peak strengths and η

η	$\Delta E/E_0$		
	Experiment	WARP	1-D theory
0.057	0.0056	0.006	0.0056
0.137	0.0152	0.0144	0.0179
0.226	0.0312	0.027	0.0283
0.29	0.0331	0.0328	0.0345

Figure 3.11 shows the relationship between $\Delta E/E_0$ and η based on the data in table 3.5. The experimental results show very good agreement with both WARP simulation and analytical results based on the one-dimensional cold fluid theory. All these results show that the energy perturbation peak-to-peak strength $\Delta E/E_0$ grows linearly with the current perturbation strength η , and the slope is about 0.1. Using the least square method, the slope can be calculated: for the experiment data, it is 0.127; for the warp simulation results; it is 0.119; for the one-dimensional theoretical prediction, it is 0.124. Therefore, the conclusion can be drawn that good predictions of the energy perturbation strength evolution can be derived from the warp simulation and one-dimensional cold fluid theory. For the group 3 and group 4, the current perturbation strength η is equal to 0.0226 and 0.29 respectively, which are not very small as are assumed in the linear theory. However, the velocity perturbation in our case is very small, which can therefore be treated as zero. As a result, the product of the current perturbation and velocity perturbation can still be neglected. Thus, it is reasonable to see that the linear theory agrees with our experiment and simulation results.

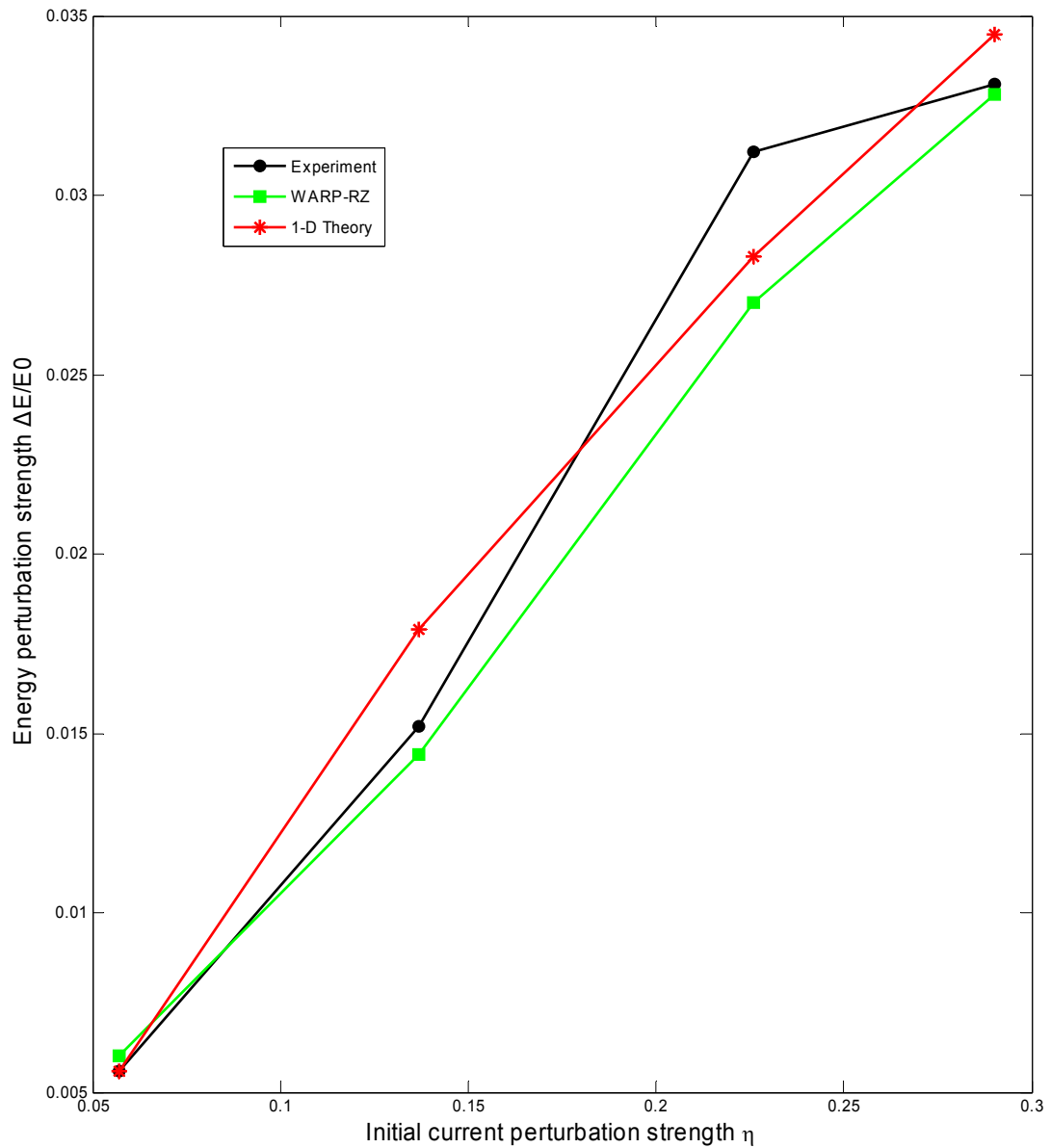


Figure 3.11 The relationship between the energy perturbation strength and initial current perturbation strength. The black dots represent experiment data, the green squares represent the WARP simulation results, the red stars represent analytical solution from one-dimensional cold fluid theory.

3.3.4 Comparisons of the space-charge wave velocity

Another important parameter for space-charge wave is the space-charge wave velocity in the beam frame c_s , which is also called sound speed. It can be calculated by equation (2.22) in Chapter 2, but a more convenient formula is:

$$c_s = \frac{v_0}{\gamma} \sqrt{\frac{1}{2} gK} \quad (3.2)$$

Where v_0 is the beam velocity; γ is Lorenz factor; g is the geometry factor and K is the generalized perveance.

Sound speed can be measured from the energy waveform, which is shown in figure by using the expression bellow:

$$2c_s = \frac{\Delta t}{\Delta z} (\beta c)^2 \quad (3.3)$$

Where Δt is the time span between the two peaks; Δz is the distance which the beam has traveled.

The theoretical results and experiment results are shown in table 3.6. The comparisons are shown in Figure 3.12. The error bars for the experiment come from the data processing method. Unlike the comparison for the energy perturbation strength, sound speed showed a big difference between the experimental results and the theoretical predictions.

The reason for this difference is not very clear at this time, but some factors may contribute to it. First, the sound speed is related to the beam radius through the geometry factor, which we calculate from the envelope equation. This may be not the

true radius. In the real beam, the radius is varying, this also can affect the value of the sound speed measured from experiment. Second, the traveling distance is only 2.3 meters, which make it difficult to locate the longitudinal position of the peaks of space-charge waves. This can also be observed in page 60 of Y. Huo's master thesis, which shows a measurement result for the separation times between two current spikes at different positions of UMER. In that case, the sound speed is calculated by the data greater than 6 meters, while the time separation near 5 meters is far smaller than the theoretical prediction. Third, during experiment the cathode in the gun is very sensitive to the vacuum conditions, while the system has some leaks due to the resistive wall current monitor at both ends of the long solenoid. So the beam is not stable enough during the experiment, which may introduce some errors such as longitudinal shift of the peaks.

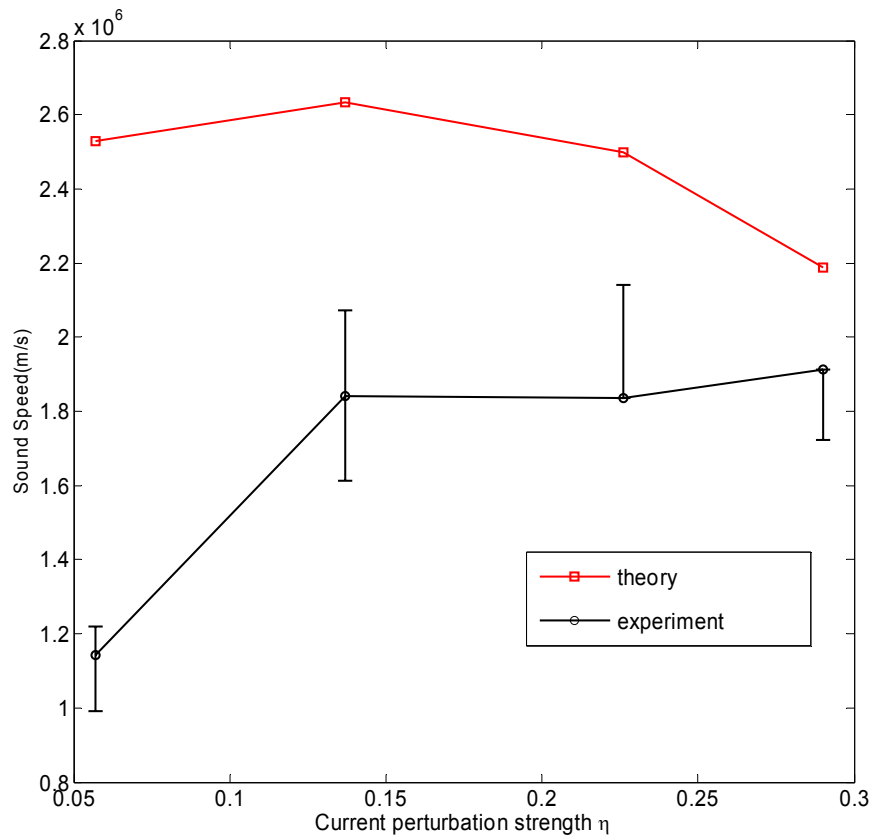


Figure 3.12 Comparison of sound speed between theory and experiment

Table 3.5 Sound speed calculated from theory and experiment

η	$c_s(\text{m/s})$ Theory	$c_s(\text{m/s})$ Experiment
0.057	2.530×10^6	1.143×10^6
0.137	2.634×10^6	1.842×10^6
0.226	2.50×10^6	1.835×10^6
0.29	2.189×10^6	1.913×10^6

Chapter 4 Conclusion

The purpose of this thesis is to study the longitudinal space-charge wave evolution in a space-charge dominated beam.

The history of space-charge wave research is reviewed first, which include some important experiments carried out in our group. Then, some basic theoretical descriptions of space-charge waves are reviewed. The first model is a simple, one dimensional, non-relativistic beam where boundary effects are ignored. With a small sinusoid initial velocity modulation, the harmonic-oscillator equation is solved. The solution shows that the modulation travels along the beam in the form of waves called space-charge waves and it is the superposition of two eigenfunctions, the fast space-charge wave and the slow space-charge wave. After that, an infinitely long cylindrical beam inside a perfectly conducting boundary is analyzed with one-dimensional cold fluid theory. The sound speed (the velocity of the space-charge wave in the beam frame) is derived by the cold-fluid model. Further, by using double Laplace transforms on the continuity equation and the momentum transfer equation in the cold-fluid model, the evolution of an arbitrary localized perturbation is solved analytically. This solution shows that if the initial current perturbation and velocity perturbation strengths are chosen properly, a single space-charge wave can be generated instead of generating by pairs. WARP simulation is performed to verify this theoretical prediction. The results show good agreement with theory.

Experiments on an initial pure current modulation evolution are also performed in the straight beam transport system in the UMER lab. This system has a

1.4-meter long solenoid after which a new generation of retarding field energy analyzer is installed. Therefore, with this experiment setup it is very convenient to study the space-charge wave evolution in a uniform focusing channel. Four groups of localized pure current perturbations with different strengths are generated by modulating the grid-voltage at the electron gun, then transporting through the matching solenoid to the uniform focusing channel. The kinetic energy of the beam is measured after the long solenoid. As the theory predicts, the space-charge waves of kinetic energy appear in pairs, one is a fast wave with a positive polarity, and the other is a slow wave with a negative polarity. In order to compare the experimental results with WARP simulation, the initial current waveforms are imported into the WARP code and the beam parameters are used consistently with the experiment. A Matlab code designed for the solution of the space-charge wave evolution for a one-dimensional cold fluid equation is also used to solve the evolution of energy perturbations for the initial current perturbations generated experimentally. The energy perturbation peak-to-peak strength is defined in order to compare the experimental results of the amplitude of the energy waves with the WARP result and theoretically analytical solution. The comparison results shows that the energy perturbation peak-to-peak strength agrees very well with the experiment, WARP simulation and one-dimensional cold fluid theory. However, the comparison of sound speed does not agree well. The possible reasons are listed and need further research.

References:

- [1] M. Reiser, Theory and Design of Charged Particle Beams, John Wiley & Sons, Inc, New York, 1994
- [2] R. Bock, IEEE Transaction on Nuclear Science, Vol. NS-30, No.4, P.3049, August 1983
- [3] C.M.Celata, Proceedings of XX International Linac Conference, P.668, Monterey, CA, 2000
- [4] Simon Yu, Proceedings of 2002 International Linac Conference, P.803, Gyeongju, Korea, 2002
- [5] J. Wei, et al, Proceedings of IEEE 2003 Particle Accelerator Conference, Portland, OR, P.571,2003
- [6] T.C.Marshall, Free Electron Laser, Macmillan Pub. Co. New York, 1985
- [7] C.K.Birdsall, and J.R. Whinnery, J. Appl. Phys., 24 P.314, 1953
- [8] A.H.W. Beck, Space-Charge Waves and Slow Electromagnetic Waves, Pergamon, New York,1958
- [9] E. Lee. Proceedings of the 1981 Linear Accelerator Confernce, Santa Fe,NM,1981
- [10] D. X. Wang, Doctoral Dissertation, University of Maryland,1993.
- [11] J. G. Wang, et al, Physical Review Letters Vol.71, P.1836, 1993.
- [12] J.G. Wang, et al, Physical Review Letters Vol.74, P.3153, 1995.
- [13] J. G. Wang, et al, Phys. Plasmas, 5, P.2064, 1998.

-
- [14] H. Suk, et al, J. Appl. Phys. 86, No. 3, P.1699, 1999.
- [15] Y. Zou, Doctoral Dissertation, University of Maryland, 2000.
- [16] D.A.Callahan, et al, Appl.Phys.,81, 3398, 1997
- [17] P.G. O'Shea, et al, Nuclear Instruments and Methods in Physics Research A 464, P. 646, 2001
- [18] UMER website: <http://www.ireap.umd.edu/umer>
- [19] Y. Huo, Master Thesis, University of Maryland,2004
- [20] Y. Cui et al, Rev. Sci. Instrm. 75, P.2738, 2004
- [21] Y. Zou et al, Phys. Rev. ST Accel. Beams 5, 072801, 2002
- [22] Y. Zou et al, Phys. Rev. ST Accel. Beams 6, 112801, 2003
- [23] Y. Cui et al, Phys. Rev. ST Accel. Beams 7, 072801, 2004
- [24] Y. Zou et al, Physical Review Letters, 94, 134801, 2005
- [25] N. A. Krall, et al, Principles of Plasma Physics, McGraw-Hill, New York, 1973
- [26] D.P.Grote et al. Fusion Eng. Des 32-33, 193-200, 1996
- [27] Private Communication with I. Haber
- [28] Y. Cui, Doctoral Dissertation, University of Maryland, 2004
- [29] J. G. Wang et al, IEEE Transactions on Electron Devices. **37**, 2622 (1990).
- [30] Private Communication with Y. Zou